Integration of indium tin oxide (ITO) with silicon for enabling electro-optical functionalities.

Author: Camiel Op de Beeck
Supervisor: prof. Pablo Sanchis Kilders
Starting date: 8/02/2016
Working group: Nanophotonics Technology Center

Objectives – The objective of this thesis is to characterize and understand the behaviour of ITO when deposited near a silicon waveguide and used as a heater for thermo-optic switching. The possibility to use ITO for optical switching is also investigated.

Methodology – First, the optical and electrical parameters of the ITO are fitted using the Drude model and a hybrid waveguide structure is simulated using modesolving software in order to gain an understanding of the structure's behaviour depending on ITO's properties. Secondly, a sample with such a hybrid ITO-near-silicon waveguide is characterized to test the simulations. Current is sent through the ITO to generate heat.

Theoretical developments – A Drude model is extracted from literature values of the refractive index to simulate the ITO. Based on the simulations, optimal configurations are found for optical modulators based on both electro-refraction and electro-absorption and for both polarizations.

Prototyping and lab work – A hybrid waveguide structure is characterized to test it's use as a heater for optical switching. Only DC analysis was done. The results are opposite to what would theoretically be expected. Extra measurements were done to try to find the cause of this behaviour. The generated heat appears to permanently change the structure.

Results – The simulations yield very compact (down to 2 µm long) electro-refractive modulators with an extinction above 6 dB. High absorption contrasts were obtained in the electro-refractive modulators. The experiments indicate that the structure is changed permanently due to the heat. The ITO appears to be undergoing a new annealing step.

Future lines – To use ITO as a heater for optical switching, the preprocessing should result in a thermally invariant ITO layer with a high resistivity.

Publications – An abstract was submitted to the Spanish Nanophotonic Conference (CEN 2016), which took place at UPV.

Abstract – Indium tin oxide (ITO) is a well known example of a transparent conducting oxide (TCO). Its electrical and optical properties have previously been extensively studied. ITO has been used for fast optical modulation based on the plasma dispersion effect. Electrical gating has been employed to substantially increase the refractive index and extinction factor of ITO in a small accumulation layer. Often, in an attempt to increase the efficiency of these devices, the proposed structures became hard to fabricate. In this paper, we simulate simple electro-absorptive (EAM) and electro-refractive (ERM) modulator structures based on the plasma dispersion effect, assuming bulk changes in ITO's carrier density. Significantly higher figures of merit have been obtained for EAMs (absorption contrasts $\sim$ 200) and very short active lengths (below 2 μm) have been found for a TM ERM. Apart from optical modulation, ITO's conducting properties suggest its use as an efficient heater for thermo-optic switching. A sample has been fabricated using high throughput methods. An MZI structure on the sample has demonstrated behaviour opposite to what could be expected from the thermo-optic effect in silicon. The influence of long term heating on the sample has been investigated and characterized.

Author: Camiel Op de Beeck, email: opca@teleco.upv.es
Supervisor: prof. Pablo Sanchis Kilders, email: pabsanki@dcom.upv.es
Delivery date: July 9, 2016

Contents

1 Introduction **1**

2 Theory & Simulations **1**
2.1 Optical properties of ITO and the influence of the free carrier density . . 1
2.2 Modulation using ITO . . . 4
2.3 Optimizing the structure for modulation . . . 6
2.3.1 Figures of merit . . . 6
2.3.2 Optimization algorithms . . . 7
2.4 Fabrication aspects . . . 12
2.4.1 Conductivity mechanisms in ITO . . . 12
2.4.2 Effects of processing atmosphere and annealing . . . 13
2.4.3 Hydrogen silsesquioxane . . . 14
2.4.4 Structure fabrication . . . 15
2.5 Carrier density tuning mechanisms in ITO . . . 18
2.5.1 Capacitive structures . . . 18
2.5.2 P-N junctions . . . 20
2.5.3 N^+-N junctions . . . 21
2.5.4 Carrier generation by UV . . . 21
2.6 Switching using ITO . . . 21
2.6.1 Thermo-optic switching . . . 21
2.6.2 Non-volatile switching . . . 22

3 Experimental work **22**
3.1 Influence of the annealing temperature on the resistivity . . . 22
3.2 I-V relation . . . 22
3.3 Influence of current on the optical response . . . 24

4 Discussion **29**
4.1 Hypotheses . . . 29
4.2 Problems . . . 30
4.3 Future lines . . . 31

5 Conclusion **33**

Acknowledgements **33**

Bibliography **33**

A Publications **37**

1 Introduction

Transparent conducting oxides (TCOs) are semiconductors with an interesting combination of characteristics: good optical transparency in and below the visible frequency range due to a large bandgap while having a high electrical conductivity, unlike most semiconductors. A well known example is indium tin oxide (ITO), for which transparencies over 80% in the whole visible range and part of the near infrared are common. These two properties are exploited in applications such as photovoltaics, liquid crystal displays and touchscreens, where TCOs are used as transparent electrodes. They provide ohmic electrical contacts without the optical losses and reflections associated with metal electrodes. The high transparency of these materials in the near infrared around 1550 nm also allows their integration in optical waveguides with low losses. Fast optical modulation is possible by exploiting the plasma dispersion effect, i.e. the dependence of loss and refractive index on the local carrier concentration. In this thesis, the optical properties of ITO are simulated based on a Drude model and the possibilities to use this material in optical modulators are investigated with basic theory. Furthermore, we propose the use of ITO as an efficient heater for thermo-optic switching. The ITO is used as a resistor in which generated Joule heat can be controlled through the current flow. To the best of our knowledge, this has not been proposed before. A fabricated sample with ITO deposited on top of SOI waveguides and MZI structures is tested to characterize the ITO's influence on the waveguide modes and its efficiency as a heater.

2 Theory & Simulations

2.1 Optical properties of ITO and the influence of the free carrier density

ITO is a heavily N-doped (degenerate) semiconductor. Reported values of ITO's bandgap differ roughly between 3.5 and 4.5 eV [1, 2]. Its permittivity is well described by Drude's model for wavelengths beyond $1\,\mu\mathrm{m}$, since its optical properties are mainly determined by the response of the electrons in the conduction band [3]:

$$\epsilon_r = \epsilon_\infty - \frac{\omega_p^2}{\omega \cdot (\omega + j\gamma)} = \left(\epsilon_\infty - \frac{\omega_p^2}{\omega^2 + \gamma^2}\right) + \left(\frac{\gamma\omega_p^2}{\omega(\omega^2 + \gamma^2)}\right) j \tag{1}$$

$$\omega_p = \sqrt{\frac{Nq^2}{m^* \epsilon_0}} \tag{2}$$

$$\rho = \frac{m^* \gamma}{Ne^2} \tag{3}$$

Here, ϵ_∞ is the long wavelength limit of the permittivity, ω_p the plasma frequency, γ the electron scattering frequency, ρ the resistivity, N the free carrier density, q the elementary charge and m^* the effective electron mass. The permittivity of ITO is thus clearly dependent on the carrier density inside, this is called the plasma dispersion

effect. The carrier density is assumed to be above $1 \cdot 10^{19}$ cm^{-3}. Below this value, ITO is no longer conducting and behaves as a Mott insulator [4]. We adopt values from the literature for ϵ_∞, m^* and the complex refractive index at $\lambda = 1.55\,\mu\text{m}$. From this value of the complex refractive index, the carrier density and scattering frequency can be estimated. Since $\epsilon_r = (n + j\kappa)^2$, we can write expressions for the real and imaginary part of the refractive index as a function of the Drude parameters:

$$n = \sqrt{\frac{1}{2}\left[\epsilon_\infty - \frac{\omega_p^2}{\omega^2+\gamma^2} + \sqrt{\left(\epsilon_\infty - \frac{\omega_p^2}{\omega^2+\gamma^2}\right)^2 + \left(\frac{\gamma\omega_p^2}{\omega(\omega^2+\gamma^2)}\right)^2}\right]} \tag{4}$$

$$\kappa = \frac{\gamma\omega_p^2}{2\omega(\omega^2+\gamma^2)} \cdot \frac{1}{n} \tag{5}$$

This 2x2-system is solved for the electron scattering frequency, the plasma frequency and thus the carrier density. From the model we can also extract the angular frequency at which the modulus of the permittivity is minimal. This is called the epsilon-near-zero (ENZ) frequency. It is more relevant than the plasma frequency for a material of which the background permittivity is not unity. The analytical expression of the ENZ-frequency is the following:

$$\left.\frac{\partial|\epsilon_r|}{\partial\omega}\right|_{\omega_{\text{ENZ}}} = 0 \tag{6}$$

$$\omega_{\text{ENZ}} = \frac{\omega_p}{\sqrt{\epsilon_\infty}} \cdot \sqrt{\frac{1 + \sqrt{1 + 2\epsilon_\infty \frac{\gamma^2}{\omega_p^2}}}{2}} \simeq \frac{\omega_p}{\sqrt{\epsilon_\infty}} \tag{7}$$

All these parameters are summarised in table 1.

Parameter	Symbol	Value
Background permittivity	ϵ_∞	3.9 [3]
Effective electron mass	m^*	$0.35 \cdot m_e$ [5]
Complex refractive index	$n + j\kappa$	$1.6761 + 0.11j$ [6]
Electron scattering frequency	γ	$4 \cdot 10^{14}$ Hz
Bulk electron density	N	$2 \cdot 10^{20}$ cm^{-3}
Plasma wavelength	$\lambda_p = \frac{2\pi c}{\omega_p}$	$1.39\,\mu\text{m}$
ENZ wavelength	$\lambda_{\text{ENZ}} = \lambda_p \cdot \sqrt{\epsilon_\infty}$	$2.76\,\mu\text{m}$
Resistivity	ρ	$2.53 \cdot 10^{-3}$ Ω·cm

Table 1: Optical and electrical parameters of ITO. m_e is the electron mass.

The approximation in equation (7) is valid when $\gamma << \omega_p$. In our case, the deviation is 7%. The approximation is valid and thus used. ITO's optical properties (permittivity, index and ENZ-wavelength) are summarized in figure 1 as a function of the free carrier density, under the assumption that the electron scattering frequency is the same..

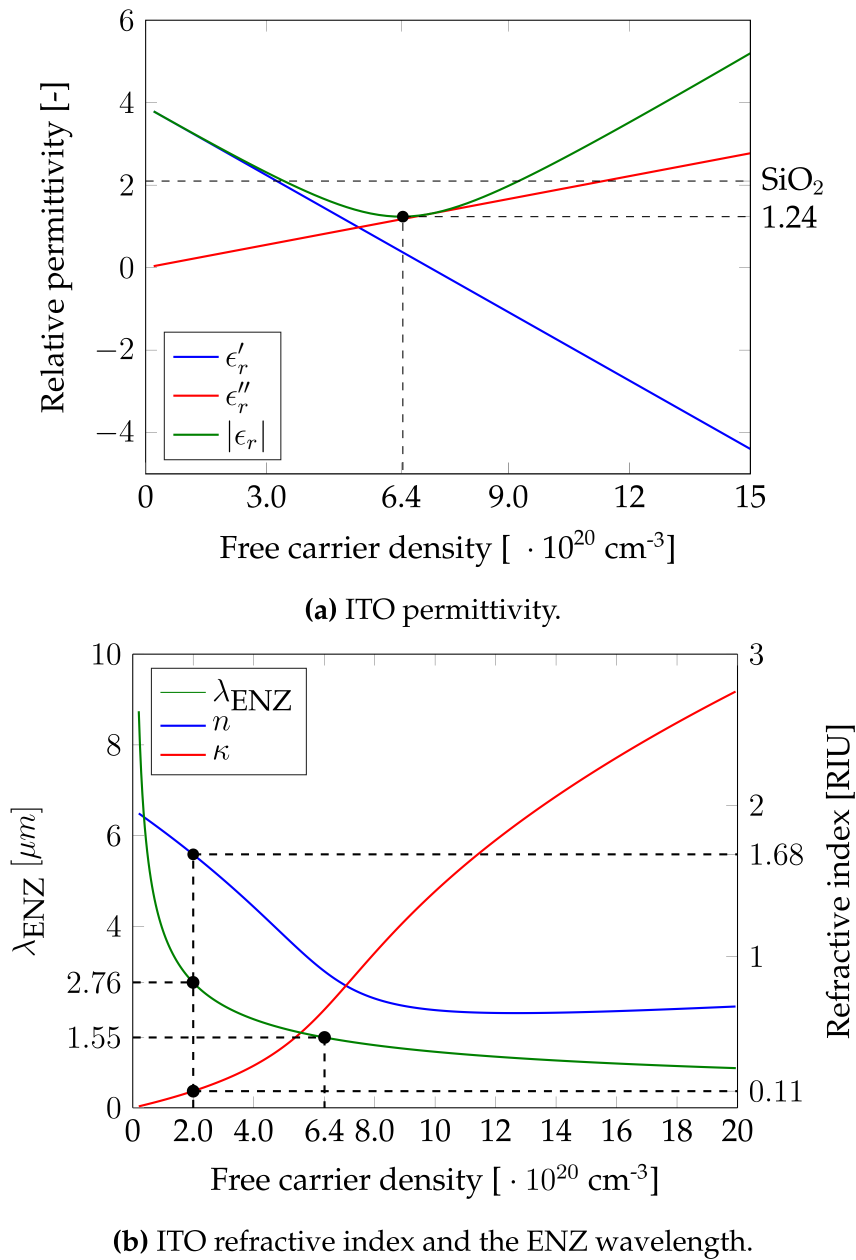

(a) ITO permittivity.

(b) ITO refractive index and the ENZ wavelength.

Figure 1: Influence of free carrier density on the optical properties of ITO at $1.55\,\mu m$.

It can be noted that the refractive index experiences a shift of around 1 refractive index unit (RIU) when the carrier density changes from a low value ($N \sim 10^{19}$ cm^{-3}) to a higher value ($N \simeq 10^{21}$ cm^{-3}). After this shift it saturates. Simultaneously, due to free carrier absorption in the conduction band of the ITO, the attenuation constant increases with the free electron density. The lowest obtainable value for the permittivity depends on the electron scattering parameter γ. In the limit of $\gamma = 0$, the permittivity is purely real and becomes zero at the ENZ frequency. At this frequency a transition would occur from perfect electric conductor to lossless dielectric. Since $\gamma > 0$, ITO is neither a lossless dielectric above ω_{ENZ}, neither a perfect conductor below ω_{ENZ}. The value of γ depends on the deposition conditions of the ITO.

2.2 Modulation using ITO

If one can place ITO in the vicinity of a silicon waveguide with the ability to tune the carrier density inside it, both electro-refractive as electro-absorptive modulation become possible since the modal index and attenuation will be influenced by the changes in the ITO. The actual mechanisms to change the carrier density will not be discussed here, for now we assume that arbitrary homogeneous carrier concentrations can be obtained such that the ITO has a uniform refractive index. Furthermore, surface behaviour is ignored. The cross-section of a basic hybrid waveguide structure is shown in figure 2. It consists of the standard 500 nm by 220 nm silicon waveguide with a silica cladding, on top of which a layer of ITO is deposited. Although silicon waveguides with this width have three guided modes (fundamental TE, TM and 1st order TE), they have lower losses for the TM mode. This is preferred to operate at both polarizations. Although there are three guided modes in the structure, we will only consider the fundamental TE and TM modes. Since the shape of TE modes is hardly altered by the ITO, mode coupling can be ignored.

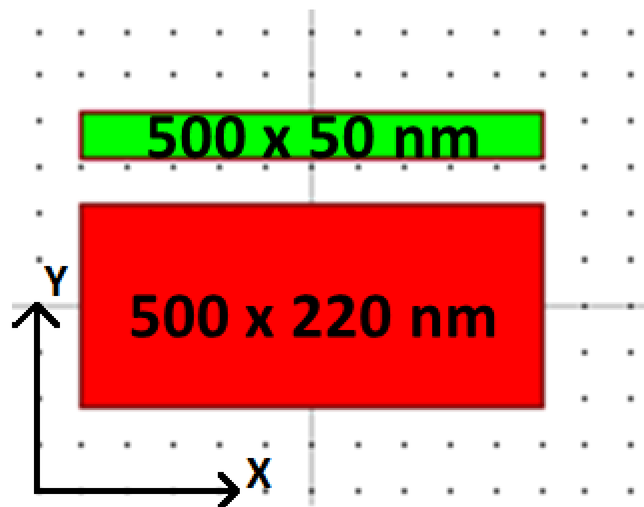

Figure 2: Basic hybrid waveguide: a layer of ITO (green) deposited on a silicon (red) waveguide with a silica spacer (here 50 nm).

In order to increase the modulation efficiency, the modal overlap with the ITO should be made as large as possible in at least one of the two states of the modulator. Here, the relatively low permittivity of ITO as compared to silicon can be exploited. Maxwell's equations dictate that the normal component of the dielectric displacement should remain continuous at an interface. For the y-component of the electric field at the SiO_2-ITO interface, this implies the following:

$$E_{y,ITO} = \left| \frac{\epsilon_{SiO_2}}{\epsilon_{ITO}} \right| E_{y,SiO_2} \tag{8}$$

The y-component of the electric field at the low permittivity side of the interface is $\left| \frac{\epsilon_{high}}{\epsilon_{low}} \right|$ times larger than at the high permittivity side. For the quasi-TM-modes of the structure, the major component of the electric field can be "drawn" into the thin ITO

layer by tuning its permittivity to the minimal value. Since this minimal value is lower than that of silica, the mode becomes more concentrated in the ITO. A slot waveguide is formed outside the silicon. The effect would be stronger if the ITO is directly deposited on the silicon. The permittivity ratio could then go up to 10 instead of 1.7 for the silica-ITO interface and the slot effect would be stronger. According to our fitted Drude model, ITO's permittivity is smaller than that of silica for bulk carrier densities between $3.5{\cdot}10^{20}$ cm^{-3} and $9.25{\cdot}10^{20}$ cm^{-3} at 1550 nm. Using a commercial mode solver software [Synopsys, RSoft: FEMSIM], the modes of the structure in figure 2 were calculated. In figure 3, the major component of the electric field is displayed for the fundamental TE- and TM-mode. In figure 4, the E_y-component of the first TM mode is displayed for 2 higher carrier densities.

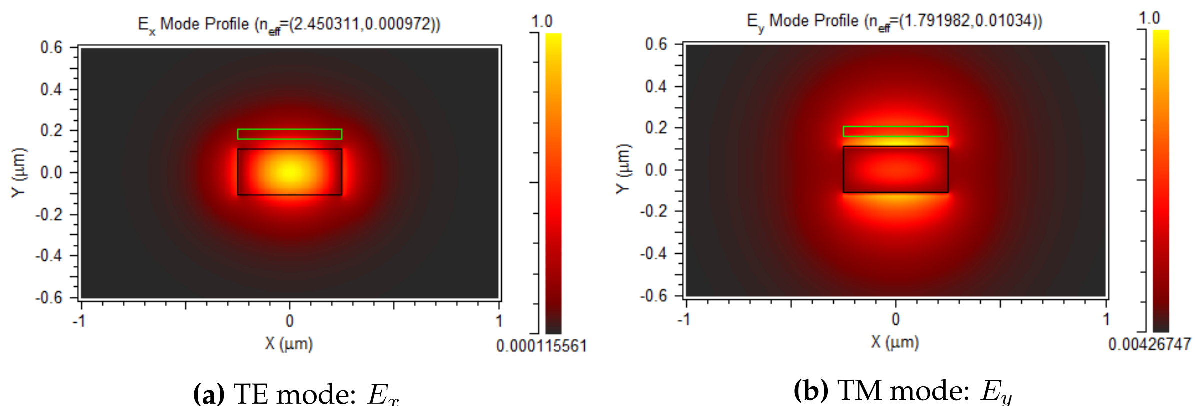

(a) TE mode: E_x **(b)** TM mode: E_y

Figure 3: Original fundamental mode profiles at 1550 nm: $N = 2 \cdot 10^{20}$ cm^{-3}

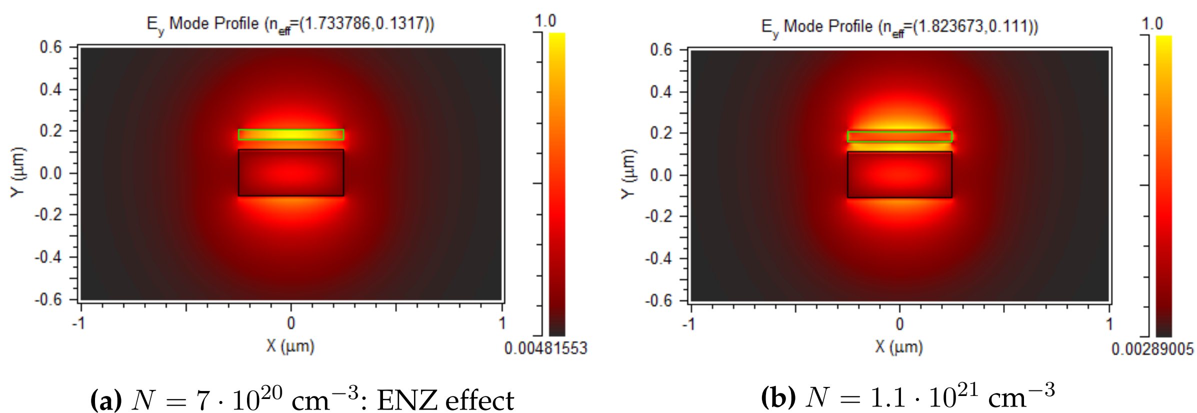

(a) $N = 7 \cdot 10^{20}$ cm^{-3}: ENZ effect **(b)** $N = 1.1 \cdot 10^{21}$ cm^{-3}

Figure 4: E_y-profiles of the first TM mode at 1550 nm with higher carrier densities.

When the difference with silica's permittivity is big enough, the optical mode is basically converted from an index guided silicon waveguide mode to a silica-ITO-silica slot waveguide mode. Increasing the carrier density above $9.25 \cdot 10^{20}$ cm^{-3} results in a silicon-silica-ITO slot waveguide, where the field is concentrated in the silica. These transitions between index guided to slot waveguide can be seen in figures 3 and 4. In figure 5, the dependence of the modal index and absorption on the carrier density are

plotted. The TE-mode is unaffected by the boundary condition on the normal component of the dielectric displacement at the silica-ITO interface, whereas the influence on the TM mode is clearly visible. The power loss in $\frac{dB}{\mu m}$ is calculated from the modal absorption factor κ using the following formula:

$$\alpha \left[\frac{dB}{\mu m}\right] = 20 \log(e) \cdot \frac{2\pi}{\lambda[\mu m]} \cdot \kappa \tag{9}$$

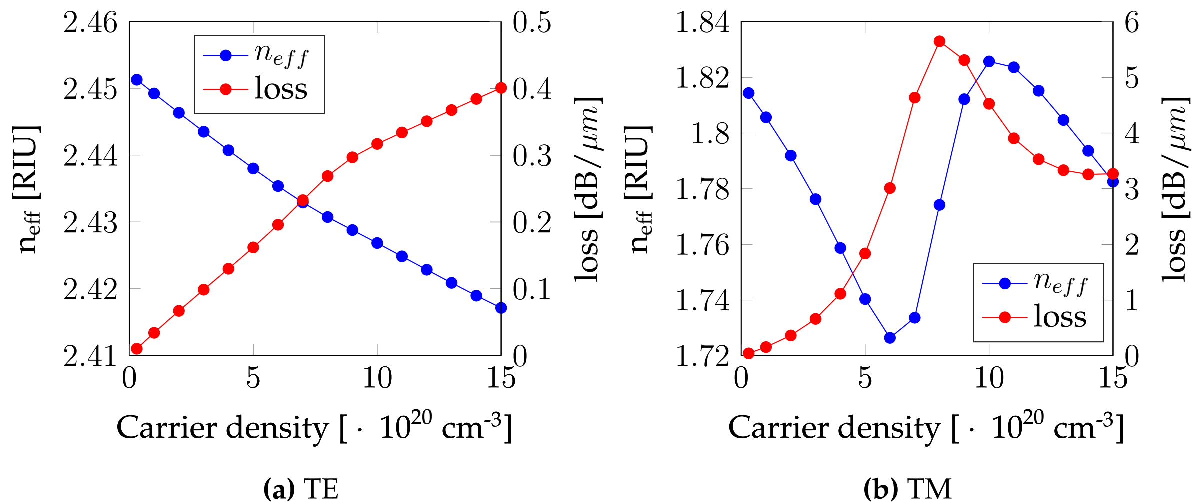

(a) TE **(b)** TM

Figure 5: Carrier density dependence of the fundamental modes at 1550 nm.

For the TE-mode, the modal shape remains almost the same for all carrier densities and the modal index and absorption simply fall, resp. rise with carrier density since part of the mode overlaps with the ITO. For the TM-mode, the slot effect results in an absorption peak near the ENZ point and also changes the refractive index of the mode around 0.1 RIU. The lowest effective index is obtained around $N = 6 \cdot 10^{20}$ cm^{-3}, which is near the point of lowest permittivity. After this point, the field is drawn less into the ITO, although the index of the latter keeps decreasing. The net effect is a renewed rise of modal index. At carrier densities above $N = 9 \cdot 10^{20}$ cm^{-3}, the slot-effect is reversed and now the silica has the lowest permittivity. Increasing the carrier density further now concentrates the field in the silica.

2.3 Optimizing the structure for modulation

2.3.1 Figures of merit

The waveguide shown in figure 2 is not optimized for modulation. Depending on the modulation mechanism (electro-refractive modulators (ERM) / electro-absorptive modulators (EAM)), different figures of merit (FOMs) can be defined and the structure has to be redesigned to for example lower the insertion losses (IL), increase the extinction ratio (ER), maximize the phase shift. . . . In order to keep the structure easily manufacturable, the simple design from figure 2 will be adopted and adjusted. The five parameters that will be optimized are the width and thickness of the ITO layer,

the size of the silica spacer and the carrier densities for both states of the modulator. One of the two states in the modulator should be one with the lowest carrier density possible (above 10^{19} cm^{-3}), since in this state the ITO has the highest refractive index and the lowest losses. Those two properties will be transferred to the modal index and absorption. A carrier density of $N = 3 \cdot 10^{19}$ cm^{-3} is chosen for the low loss state, since this value is also found in literature [7]. Now four parameters remain to be determined. For the absorptive modulators, the following figure of merit is commonly used to optimize the structure [8]:

$$\text{FOM}_{EAM} = \frac{\alpha_{max} - \alpha_{min}}{\alpha_{min}} \tag{10}$$

Here the subscripts 'max' and 'min' indicate the highest and lowest of the losses of the two states between which the modulator will switch in an on-off keying (OOK) modulation scheme. This means that the optimal structure has a high extinction ratio and low insertion losses. For the ERM, the optimal structure allows a large phase shift with low losses in both states. This is needed in order to have a large extinction in a Mach-Zehnder interferometer (MZI) structure. Two plots are given for each refractive modulator, the index difference and the insertion loss. From the latter, the needed active device length is calculated as $L_i = \lambda/2\Delta n$. The insertion loss is calculated using this length. The generally used figure of merit for ERMs, $V_\pi \cdot L$, cannot be determined, since the mechanisms to tune the carrier density are not discussed here. Instead, the induced loss in the modulation arm will be minimized, or in other words, the inverse of this loss is proposed as a figure of merit for the TE modulators:

$$\text{FOM}_{ERM} = \frac{1}{\alpha_{max} \cdot L} = \frac{2\Delta n}{\alpha_{max} \cdot \lambda} \tag{11}$$

One can then decide which feature (device length or losses) is more critical and should be minimized.

2.3.2 Optimization algorithms

We propose two different approaches to optimize the modulator. One is to try to find an optimal configuration with all four remaining parameters, the other is to fix one parameter and to perform a full 3D sweep over the three remaining parameters. If the former, we sweep the physical dimensions (ITO width and size and oxide spacer) versus the carrier density and investigate the 2D plots of the FOMs. One carrier density is chosen at which all parameters show a good performance. The dimensions that give a maximal performance are then chosen independently. The influence of the parameters on each other is ignored in this algorithm and the resulting configurations are not guaranteed to be the optimal ones in terms of the FOMs. To illustrate this algorithm, the simulations of the absorptive modulator for the TM polarization are shown in figure 6. It is obvious that the performance is optimal at the carrier density $N = 9 \cdot 10^{20}$ cm^{-3} in the plots showing gap and ITO width influence, so we will choose this as the high carrier density state. At this carrier density, neither gap and width have a big influence on the FOM, but the thickness yields a maximum at 90 nm. This is how the parameters are chosen in this algorithm. The resulting configurations and their calculated

performance as a modulator are given in table 2. For the ERMs, extinctions above 6 dB are obtained, for insertion losses below 3.5 dB. The active lengths of the modulator are relatively small as compared to other technologies, with an active length of 2.05 µm for the TM refractive modulator. Absorption contrasts in the EAMs exceed 150 for both polarizations. These results are not guaranteed to be the absolute optimal configurations, so further improvement is possible.

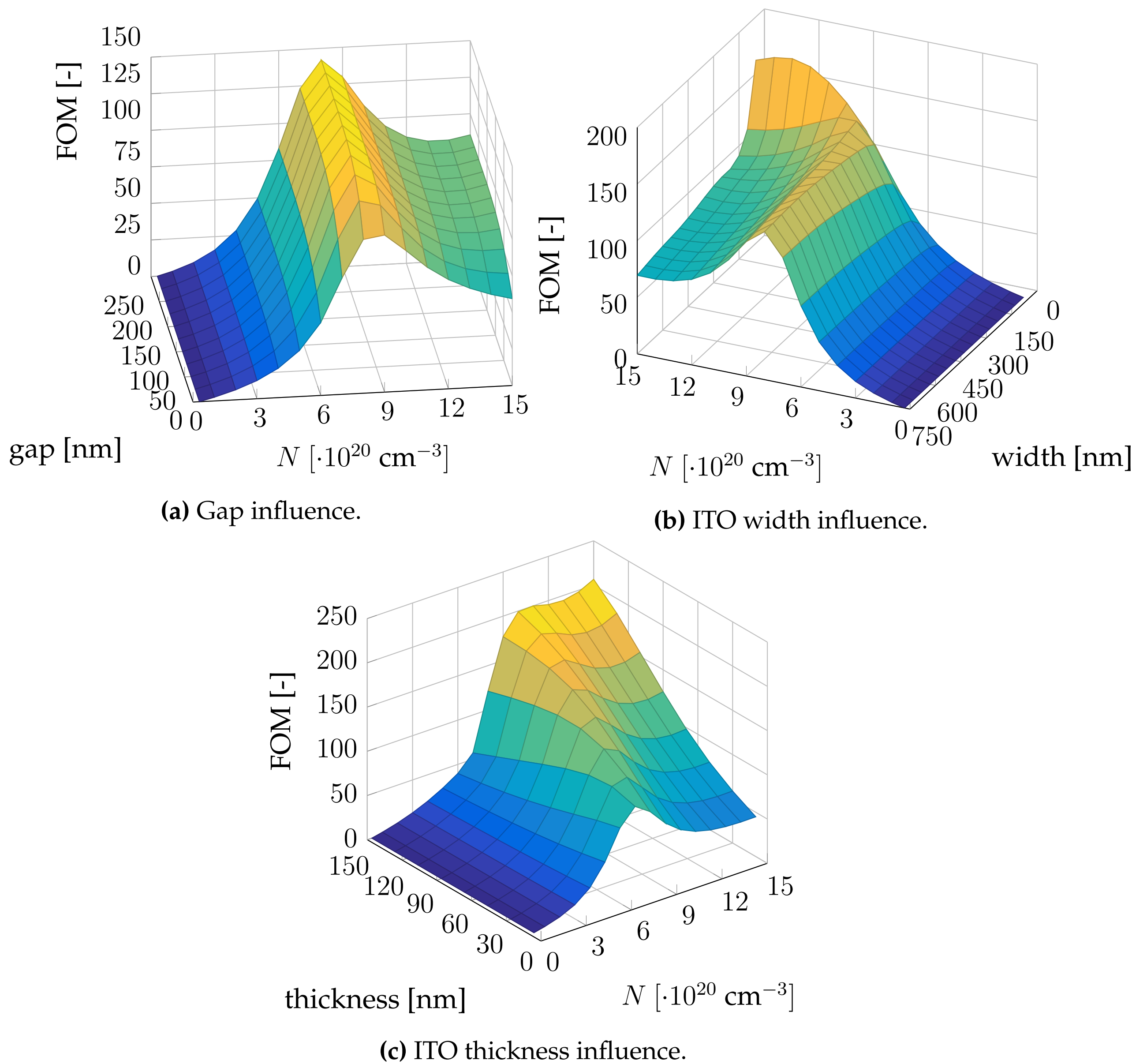

(a) Gap influence.

(b) ITO width influence.

(c) ITO thickness influence.

Figure 6: Parameter influence on TM absorptive modulator.

The second optimization is done by fixing one parameter. For ease of fabrication, it is convenient that all ITO layers on the wafer have the same thickness. This way, a single sputtering step suffices. To this purpose, optimizations are done, fixing the ITO thickness at 100 nm. A full 3D sweep is performed and at each carrier density for each polarization, the optimal ITO width and silica spacer size are determined. In fig-

Optimized for $\Downarrow$		w - t - g	FOM	N	IL [dB]	L_i [µm]	ER [dB]
Refractive	TE	500 - 150 - 0	0.115	6	3.49	12.9	6.65
	TM	500 - 150 - 0	0.115	6	3.43	2.05	6.75
Absorptive	TE	50 - 50 - 0	156	11			
	TM	550 - 90 - 100	178	9			

Table 2: Chosen parameters for the modulators, the highest achievable FOM and the ITO bulk carrier density at which it is achieved according to the first optimization algorithm. All dimensions - width (w), ITO thickness (t) & gap (g) - are given in nanometers. Carrier densities are given in units of 10^{20} cm^{-3}. For the ERMs, the IL, ER and needed active length to reach a phase shift of π of the modulator are given.

ure 7, the maximum obtainable FOMs are plotted over the simulated carrier densities. The FOMs are still calculated assuming that the carrier density in the low loss state is $3 \cdot 10^{19}$ cm^{-3}. In figure 7a, the ENZ-peak can be observed for the TM absorptive modulator as expected. The TE-mode experiences a similar peak around the ENZ-regime, however the needed configuration is completely different. According to the simulations, a wide ITO layer is needed to maximally exploit the ENZ effect for the TM polarization, whereas in the TE case, only a very narrow ITO layer is needed. From figure 7b, we could conclude that the optimal configuration for a TE refractive modulator is a wide ITO deposition at a large distance from the waveguide, although from figure 10b, it is obvious that the gap only has a minor influence on the FOM. In fact, at higher values of the width, the ratio $\frac{\Delta n}{\alpha_{max}}$ remains almost the same and the actual shape of the structure does not influence the performance of the TE ERM. The FOM for the TM refractive modulator drops off at higher carrier densities since the influence of the ITO's losses outweighs its decrease in refractive index. The optimized configurations and their characteristics are given in table 3. For the ERMs, the obtained extinction ratios and insertion losses are similar to the ones obtained in the first algorithm, although the active lengths are now significantly larger. The losses outweighed the active length in the FOM, so a more "weighted" FOM might be used to obtain a more compact structure with more losses or a longer structure with less losses. The absorption contrasts in the EAMs are larger than those from the first algorithm.

In figures 8, 9 and 10, the criticality of the gap and width is checked for the most important configurations from figure 7, i.e. those who offer the best performance in a broad range of carrier densities. Structures that offer an optimal performance even when the dimensions are changed in the deposition are better suited for fabrication. The shape of these plots remains more or less the same over their indicated range, such that only one plot is shown for each configuration. In figure 8, comparing the two plots for the absorptive TM modulator, it would appear that the width of the ITO layer is a critical parameter of the optimal structure at high carrier densities, as seen in figure 8a. On the other hand, the maximum in figure 8b is rather broad and insensitive to both gap and width variations. Comparing the two main configurations of the TE absorptive mod-

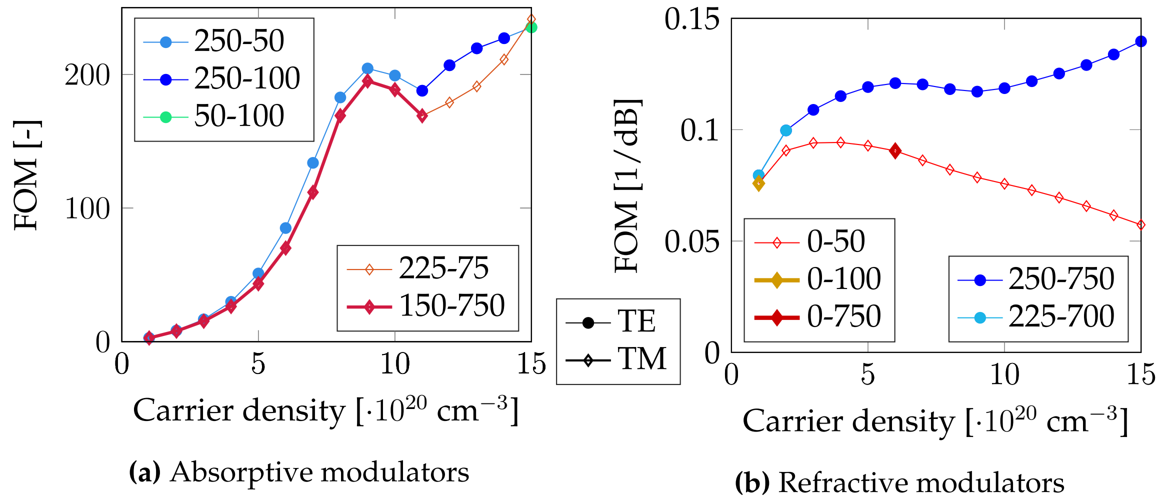

(a) Absorptive modulators

(b) Refractive modulators

Figure 7: Optimal FOMs and the configurations at which they are reached. The legends indicate the gap and ITO width in nanometers (in that order) for which the maximal FOM is obtained. Colours indicate different configurations, the symbol indicates the polarization.

Optimized for ⇓		w - t - g	FOM	N	IL [dB]	L_i [µm]	ER [dB]
Refractive	TE	750 - 100 - 250	0.121	6	3.19	943	7.07
	TM	50 - 100 - 0	0.094	4	3.76	29.8	5.27
Absorptive	TE	50 - 100 - 250	204	9			
	TM	750 - 100 - 150	195	9			

Table 3: Chosen parameters for the modulators, the highest achievable FOM and the ITO bulk carrier density at which it is achieved according to the second optimization algorithm. All dimensions - width (w), ITO thickness (t) & gap (g) - are given in nanometers. Carrier densities are given in units of 10^{20} cm^{-3}. For the ERMs, the IL, ER and needed active length to reach a phase shift of π of the modulator are given.

ulator in figure 9, we see that the structure is insensitive to variations of the gap. The maximum performance shifts from an ITO width of 50 nm at low carrier densities to an ITO width of 100 nm at higher carrier densities. This parameter is critical in both cases. Finally, the refractive modulators each have one configuration that is optimal at basically every carrier density. The TE refractive modulator is insensitive to gap variations and more sensitive to variations of the ITO width, similar to its absorptive variant. The maximum performance at high ITO widths is however more flat and broad and therefore less critical than in the absorptive case, as can be seen in figure 10b. The refractive TM modulator is more sensitive to the gap than to the width, and the gap should be minimized. At higher carrier densities, the performance decreases more with higher ITO widths and this parameter becomes more critical. However since this modulator would not be used at higher carrier densities due to its decreasing performance, this is not an issue. These simulations include higher values of the ITO width, showing

convergence when the dimensions approach and exceed the wavelength of the guided light.

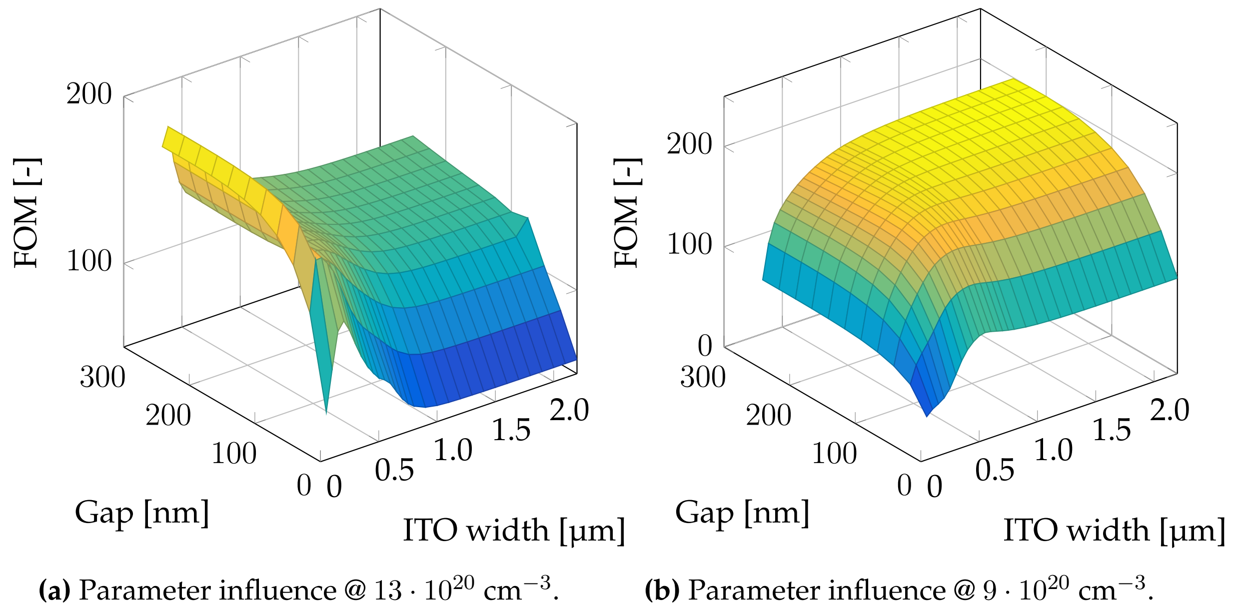

(a) Parameter influence @ $13 \cdot 10^{20}$ cm^{-3}. **(b)** Parameter influence @ $9 \cdot 10^{20}$ cm^{-3}.

Figure 8: Absorptive modulator for the TM-mode.

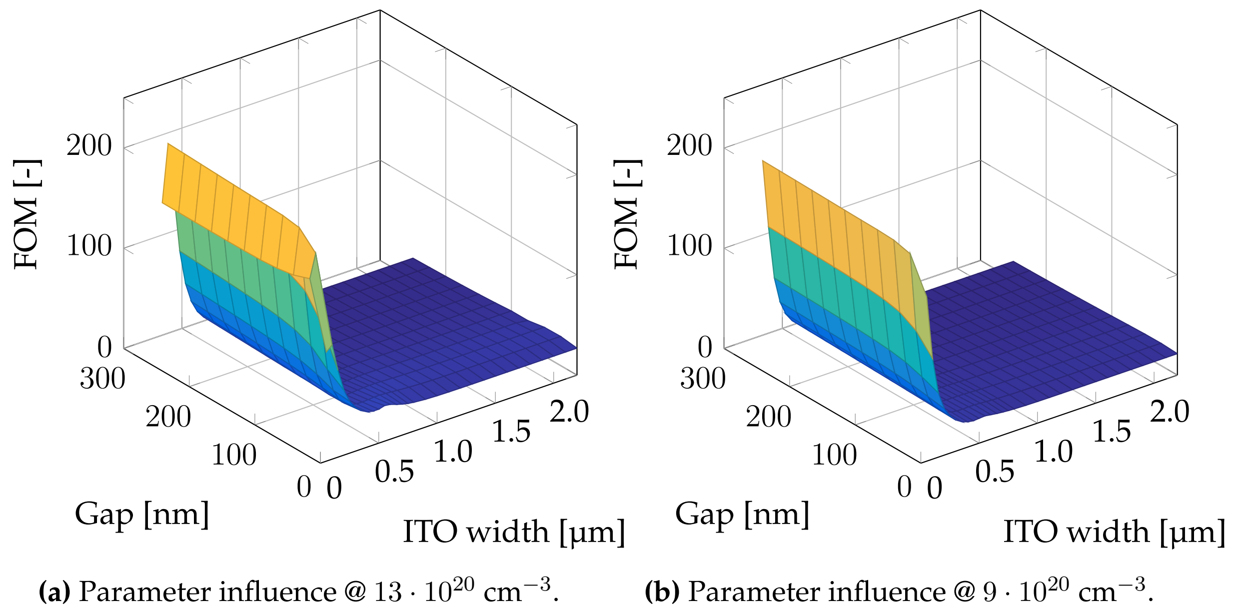

(a) Parameter influence @ $13 \cdot 10^{20}$ cm^{-3}. **(b)** Parameter influence @ $9 \cdot 10^{20}$ cm^{-3}.

Figure 9: Absorptive modulator for the TE-mode.

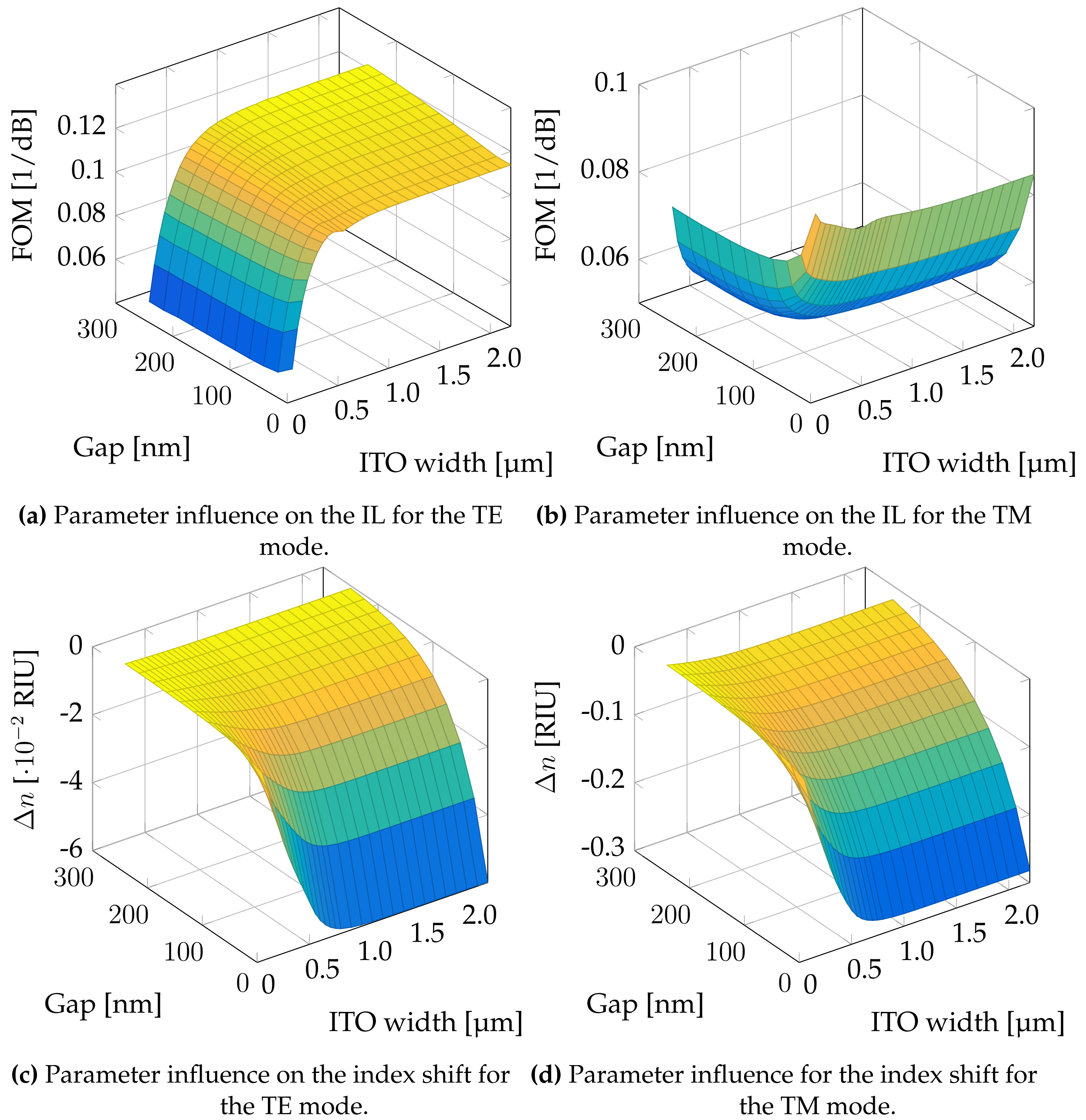

(a) Parameter influence on the IL for the TE mode.

(b) Parameter influence on the IL for the TM mode.

(c) Parameter influence on the index shift for the TE mode.

(d) Parameter influence for the index shift for the TM mode.

Figure 10: Refractive modulators @ $5 \cdot 10^{20}$ cm^{-3}.

2.4 Fabrication aspects

2.4.1 Conductivity mechanisms in ITO

As a model for ITO's crystal structure, the In_2O_3 lattice is used. In_2O_3 is considered to be the host lattice for doping with Sn. In^{3+}-ions can be substituted for Sn^{4+}-ions. The tin acts as a shallow donor, little below the conduction band. Oxygen vacancies in the In_2O_3-lattice also act as doubly charged shallow donors. At room temperature, these donor states donate their electrons to the conduction band by thermal excitation [4]. Due to the shallow doping, the high optical bandgap of indium oxide remains intact.

When the doping level increases, the donor states merge with the conduction band and the electrons form a degenerate Fermi-gas. This is the reason why ITO's optical response in the infrared can be described by a Drude model. Although the Sn^{4+}-ions and oxygen vacancies increase the carrier density, they also act as impurities onto which the electrons scatter, thus lowering the mobility. These two effects counteract, leading to resistivity extrema at certain oxygen and tin concentrations [8]. The filling of the bottom of the conduction band leads to an apparent increase of the optical bandgap. This is known as the Burstein-Moss shift, which is typical for degenerate semiconductors. The Fermi-level rises with electron density from below the conduction band at low doping to inside it at higher doping. Sato et. al. measured a downward shift of 0.5 eV in ITO's work function for a tenfold increase of the carrier density in ITO from $8.8{\cdot}10^{19}$ cm^{-3} to $8.2{\cdot}10^{20}$ cm^{-3} [9]. Brewer and Franzen have simulated ITO's properties such as Fermi energy, bandgap energy and free electron concentration as a function of the amount of Sn-substitutes in indium sites of the crystal [10]. The calculations were done using density functional theory in the assumption of a perfect bulk crystal. Their results indicate that the electron concentration does not increase indefinitely with the Sn-concentration, but reaches a maximum when the Sn/In-ratio is 0.25.

2.4.2 Effects of processing atmosphere and annealing

In this section, the influence on the crystal structure and the conductivity of the working gas in the deposition and annealing step are discussed. The presence of O_2 in the working gas during the deposition step will influence the amount of oxygen absorbed in the ITO. Depending on the concentration, both the crystal structure and the conductivity are affected. When no oxygen is present in the working gas during the deposition step, the as-deposited layer is amorphous since the crystal structure cannot be formed [11]. When a small partial pressure of oxygen is added to the working gas, crystallinity increases with O_2-concentration, as shown by Guillén and Herrero using X-ray diffraction patterns to detect periodic structures in the ITO layer [2]. The grain size in the ITO increases with O_2-pressure for a $P(O_2)/P(Ar)$ ratio below 0.008. With increasing crystallinity, the amount of grain boundaries decreases, resulting in less scattering and a higher electron mobility. Oxygen can fill in vacancies in the crystal and deactivate Sn^{4+}-donors. This results in a lower scattering frequency, but also a lowered carrier concentration. These two traits affect the conductivity in opposite ways. At a certain oxygen concentration in the deposition atmosphere, a minimal resistivity value could be expected. Such a minimal resistivity is reported by Bender et. al. for an oxygen concentration of 0.56% in the working gas, after an annealing step of 6 minutes at 200 °C in vacuum [1]. Increasing the oxygen concentration in the working gas even more will lead to the formation of insulating layers in the ITO during deposition since the stoichiometric crystal cannot absorb it. This effect, together with the fact that Ar atoms are heavier than O_2-molecules and have more collision impact on the target, explain why increasing the amount of oxygen in the working gas reduces the growth rate per unit of time. A linear decrease of the growth rate with increasing oxygen concentration (up till 25 %) in the working gas was reported by Rein et. al. [11]. Apart from composition, also total pressure influences the growth rate.

Annealing steps will generally give the atoms in the as-deposited layer more energy to relocate themselves to energetically more favourable positions. Annealing temperatures above 200 °C are found to promote grain growth and crystallization. The average grain size becomes bigger with higher annealing temperatures if the samples are annealed long enough. This manifests itself in an increasing surface roughness [12]. For the grain growth, the annealing atmosphere is not relevant, equal degrees of crystallization were reported for annealing in vacuum and air by Guillén et. al. [2]. This contributes to a higher conductivity through a higher carrier mobility. However, in an annealing step in vacuum, oxygen from the crystal may diffuse and escape into the atmosphere, reactivating Sn^{4+} sites and oxygen vacancies, resulting in an extra increase in conductivity. The same happens for an anneal in air when the oxygen concentration in the deposition step was high enough (above 5%). On the other hand, when the oxygen concentration in the deposition was low, the ITO will absorb oxygen from the air during annealing, decreasing the number of charge carriers and vacancy defects.

2.4.3 Hydrogen silsesquioxane

Hydrogen silsesquioxane (HSQ) is an inorganic compound that can be used both as a negative tone e-beam resist and for oxide layer growth. It is commercially known as FOx (flowable oxide), since it can applied to a wafer surface in a solution. The carrier solvent is usually methyl isobutyl ketone (MIBK). The solution can be distributed evenly over the wafer surface using spin coating. HSQ has a box-like molecular structure, shown in figure 11. With a baking step, the carrier solvent can be evaporated and the HSQ remains on top of the wafer in a solid form. Its molecular shape causes the deposited layer to be very porous. When heated to high temperatures, thermal dissociation occurs in the structure. The Si-H bonds are destroyed and substituted for Si-O bonds, interconnecting the different boxes. The chemical reactions describing this structural change are stated by Yang and Chen [13]. The structure becomes stronger and more similar to silica, but the boxed shape is still not destroyed so the refractive index remains below that of thermally grown silica. High temperature treatments above 350 °C irreversibly destroy the box structure and lead to a porous network structure or, at even higher temperatures (above 450 °C) to a collapse of the porous network with an appreciable volume change (10% - 15 %). Exposure to particles with sufficient energies to break the Si-H bonds, such as plasmas, electron beams and UV-light, has the same effect. Destroying the box structure reduces the solubility in the MIBK. This feature makes HSQ a suitable material to use as a negative resist. Lithography can be done using light with wavelengths below 157 nm and e-beams [14, 15].
HSQ is used to grow planar oxide layers on structures with a lot of surface height variations. Due to the fact that its deposited in liquid form, it is well suited for filling holes and gaps in structures. The HSQ layer undergoes two volume changes in its processing: one during the baking, in which the MIBK is evaporated, and one during a hard curing step. In this hard curing, the porous as-deposited HSQ is exposed to an oxygen plasma which breaks the Si-H bonds and destroys the box structure. A hard curing step of 30 minutes is sufficient to let almost all the boxes collapse. Both volume changes can be predicted and therefore the height of the final layer can be estimated and controlled quite well. In figure 12, the planarity of the deposition is shown for two

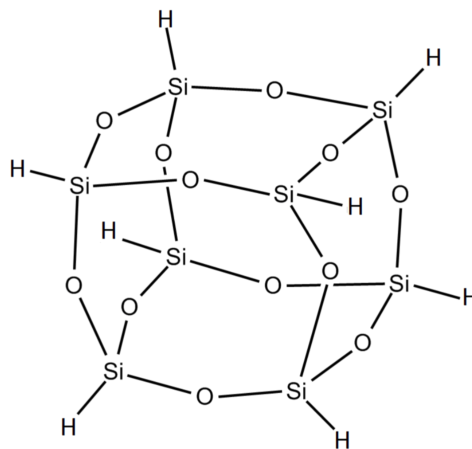

Figure 11: HSQ's box structure [16].

types of structures. The first is a wafer with two waveguides, the second is a wafer with a photonic crystal. In the former, still some surface elevation can be noticed over the waveguides, while in the latter, the oxide layer is nearly flat.

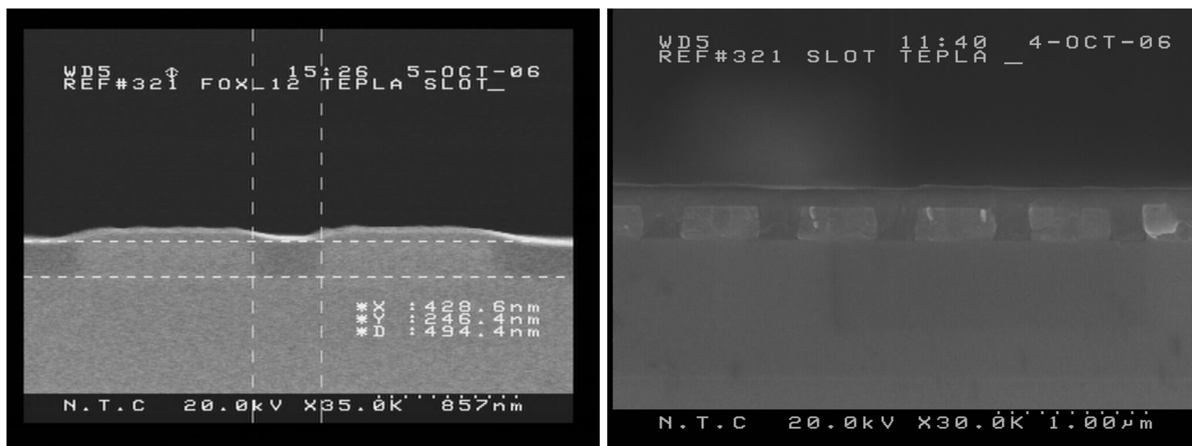

(a) HSQ deposited on top of a wafer with sparsely covered surface.

(b) HSQ deposited on top of a wafer with a photonic crystal.

Figure 12: (Quasi-)planar oxide deposition using HSQ.

2.4.4 Structure fabrication

In this section, the processing steps are discussed that were used to fabricate the tested sample, since the dependence of material properties on their deposition method is relevant in the discussion of the result. The sample contained ITO on SOI waveguides to investigate its use as a heater for optical switching. The starting point is a Si/oxide/SOI wafer with a 2 µm SiO_2 layer and 220 nm of SOI. A layer of HSQ-based negative e-beam resist [Dow Corning XR-1541-006] is deposited. The HSQ above the future waveguide is irradiated with an electron beam, reducing its solubility in MIBK. The remaining resist is dissolved and the exposed silicon is etched away. The 500 nm wide waveguides

are formed. Next, an oxide spacing layer should be grown on top of the wafer. This is typically done using plasma-enhanced chemical vapour deposition (PECVD), where Si-containing and O-containing chemicals react and attach to the wafer. The resulting oxide layer is however not flat near the silicon waveguide, the deposition is conformal, i.e. not highly directional, as shown in figure 13a. This is not ideal since the ITO would be deposited onto a curved surface and the target spacing between the ITO and the waveguide would not be reached accurately enough. Therefore oxide layer was grown using HSQ. The solution is evenly distributed over the wafer surface by spin coating, see figure 13b, and the carrier solvent is evaporated in a hard baking steps during 120 seconds at 200 °C. Since our sample has only a few sparse waveguides on its surface, it resembles figure 12a more than figure 12b. Still some surface elevation will be present, but far less than with PECVD.

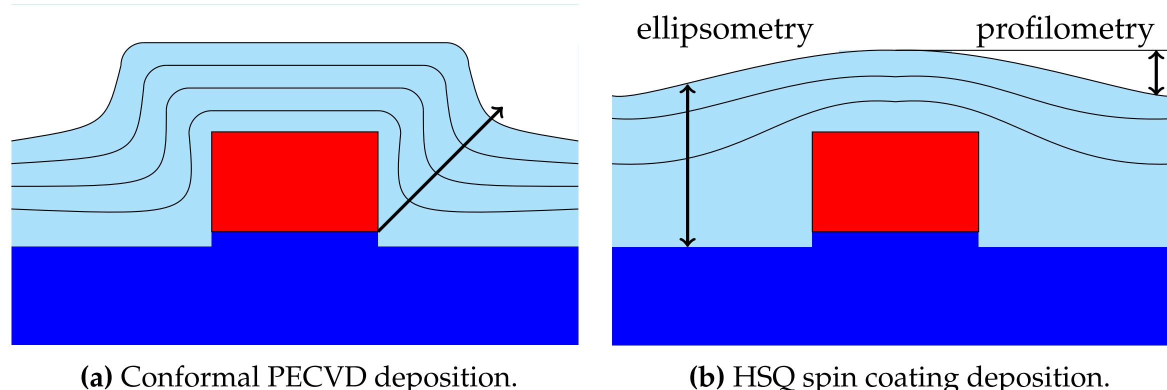

(a) Conformal PECVD deposition.

(b) HSQ spin coating deposition.

Figure 13: Comparison between oxide deposition methods and (b) experimental spacer size determination.

At this point, the HSQ molecules still have their box structure, but the different boxes are weakly connected and the deposited layer is very fragile and easily removed. Since the structure is very porous, its refractive index (1.39) is a bit lower than that of thermally grown silicon oxide (1.45). An extra hard curing step is needed to strengthen the layer. This is done by exposing the HSQ to an oxygen plasma. This removes the Si-H bonds and destroys the box structure, leading to an oxide layer more similar to thermally grown silica.

The thickness of the deposited oxide layer should now be measured in order to know more precise how far from the silicon waveguide the ITO will be deposited. This is done using ellipsometry and profilometry, as shown in figure 13b. The substrate oxide layer was originally 2 μm, but a part of it is removed due to overetching during the definition of the silicon waveguide. The thickness of the oxide layer is measured using ellipsometry before and after the deposition of the HSQ layer. Since the refractive indices of the HSQ and the substrate silica are so similar, their joint thickness can be detected as if they were a single layer. Subtracting the substrate thickness from that of the total oxide layer yields the thickness of the HSQ away from the waveguide. Profilometry is then used to find the height difference between the surface far away from

and on top of the silicon waveguide. Now, the spacing between the waveguide and the ITO layer is known.

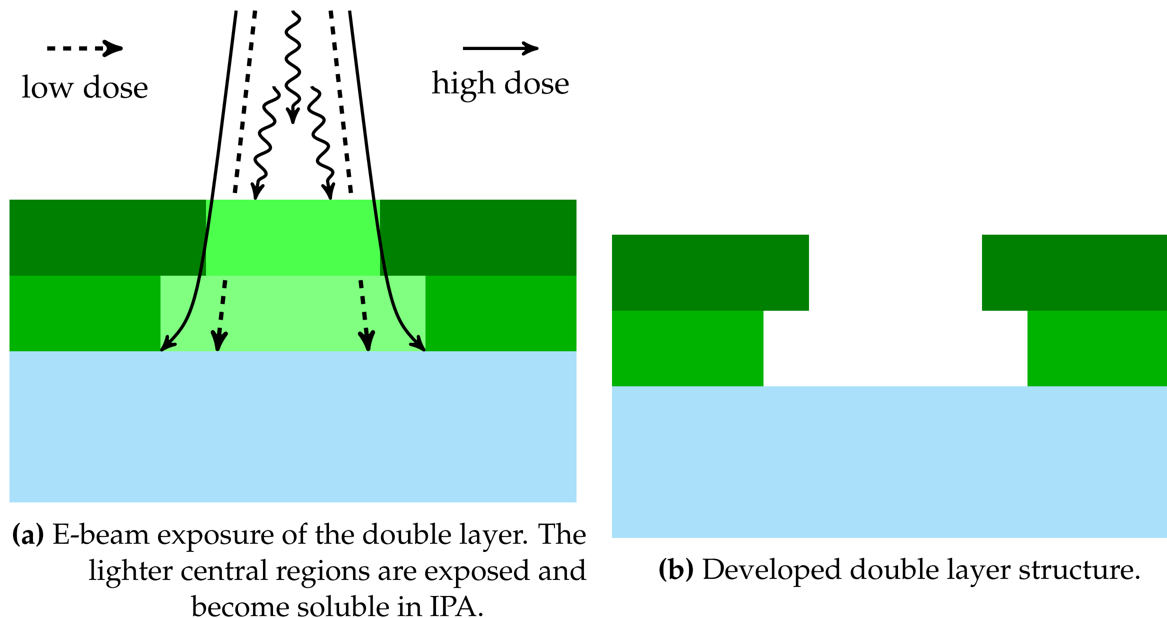

(a) E-beam exposure of the double layer. The lighter central regions are exposed and become soluble in IPA.

(b) Developed double layer structure.

Figure 14: Process of PMMA double layer development.
Blue = HSQ, lighter green = exposed PMMA, darker green, unexposed PMMA.

After the strengthening of the oxide layer, the ITO can be deposited. A layer of polymethyl methacrylate (PMMA), a positive photoresist, is spin coated on top of the HSQ and is irradiated with an electron beam where the ITO is supposed to end up. This process is shown in figure 14. The exposure to the electrons makes the PMMA more soluble in the developer fluid. A double PMMA layer is deposited using two variants with different molecular weights. The lower layer has a higher sensitivity to the electron beam than the upper layer. The PMMA is exposed to two consecutive irradiations with increasing dose. The first (low) dose develops the lower layer, whereas the upper layer needs a higher dose: the second one. This second dose also irradiates the lower region, leading to a broader affected region near the oxide layer. The exposed parts are removed using a mixture of MIKB and isopropanol (IPA). This is schematically shown in figure 15. An ITO layer is deposited on top of the wafer through DC-sputtering [Emitech K675X sputter coater] at room temperature. DC-sputtering is a commonly used deposition method due to its high throughput. The working gas in the sputtering was a mixture of argon and 8 vol% oxygen. The oxygen was introduced in the gas to increase the resistivity of the deposited ITO. This can be expected since filling in oxygen vacancies in the ITO lattice removes an ion-scattering centre, at the cost of abducting two electrons from the conduction band. The resistivity of the sample should be high such that power is dissipated mostly in the ITO and not in the rest of the circuit. The thickness of the ITO layer depends on both the sputtering time and the composition of the working gas, as explained in section 2.4.2. The used sputtering machine automatically stops and vents after 4 minutes. Using 0 vol% O_2, the sputtered thickness

after 4 minutes is around 120 nm, whereas at 8 vol% O_2, it is only around 92 nm. The remaining PMMA with ITO on top is removed by a lift-off process. Here, the reason to use a double layer becomes clear. In the configuration of figure 15a, the solvent cannot reach the PMMA, whereas in figure 15b, this is not a problem. In order to have a layer with a uniform thickness produced by this sputtering machine, the width of the layer should be around 300 nm or higher. This indicates that the simulated optimal configuration for a TE absorptive modulator is not achievable using the described fabrication method, see table 2. After the deposition, the sample was annealed at 300 °C during 30 minutes in an N_2 atmosphere. The influence of the temperature of this annealing step is given in section 3.1.

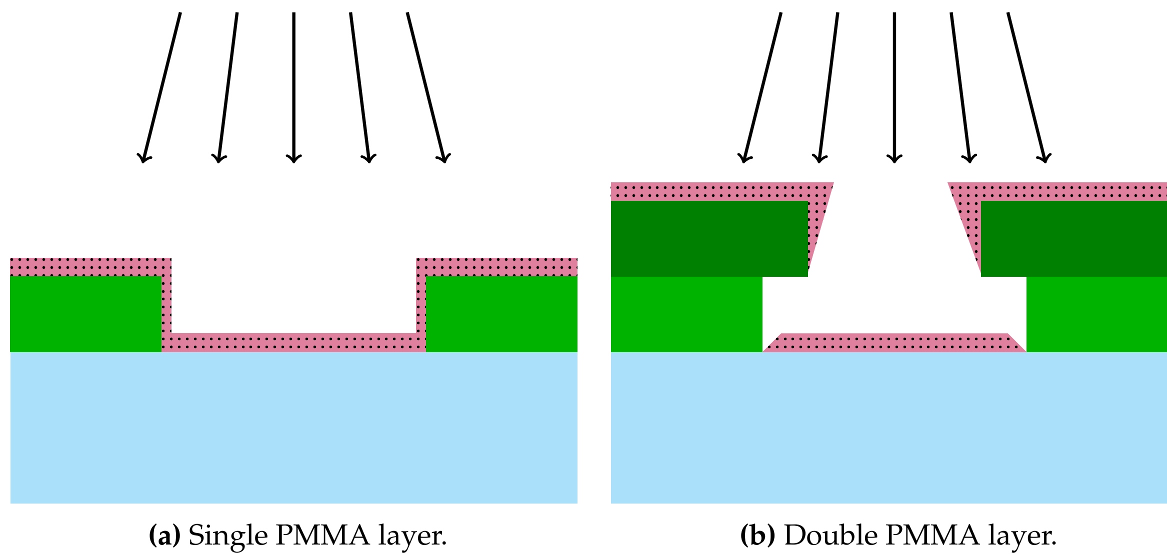

(a) Single PMMA layer. **(b)** Double PMMA layer.

Figure 15: Sputtering of ITO on the HSQ layer.
Blue = HSQ, green = PMMA, dotted purple = ITO

In figure 16, the dimensions of the simulated and fabricated structures are shown. An ITO layer of 100 nm thickness is deposited on the silicon waveguide with a silica spacer of 200 nm between them. The width of the ITO layer is 67 µm. Extra squares of ITO are added to facilitate contacting with DC-probes. Apart from the two MZI structures, 8 more straight waveguides were present on the sample: 4 with TE gratings and 4 with TM gratings including one reference waveguide without ITO on top for each polarization. The TM waveguides had ITO strips with lengths of 50 µm, 100 µm and 250 µm. The strip lengths on the TE waveguides were 250 µm, 500 µm and 1000 µm.

2.5 Carrier density tuning mechanisms in ITO

2.5.1 Capacitive structures

In the literature, most works rely on electrical gating and accumulating charge at the interface of the ITO and an insulator in order to capacitively increase the carrier density in the ITO significantly, leading it to a higher loss ENZ state at the boundary. Some

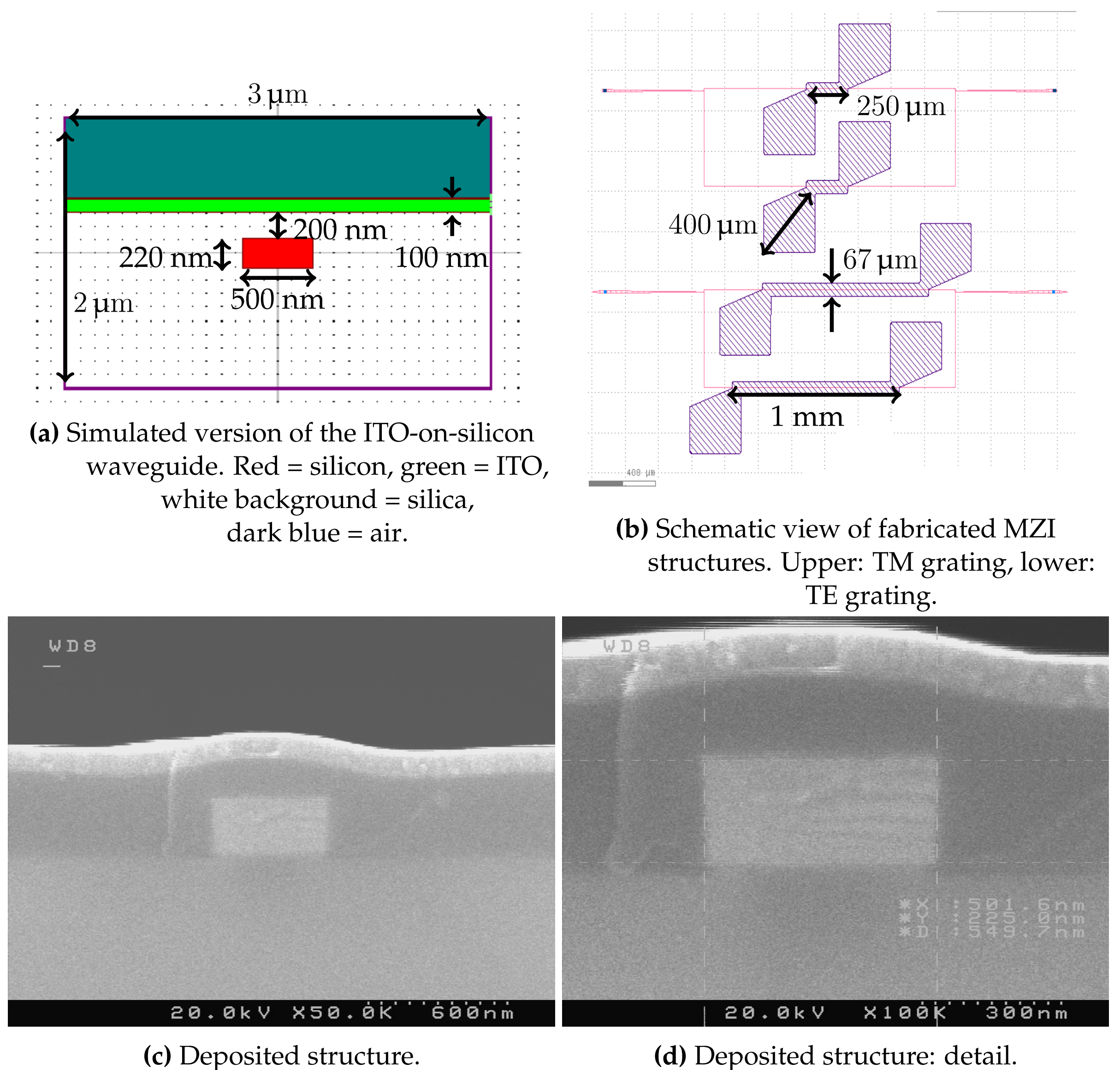

(a) Simulated version of the ITO-on-silicon waveguide. Red = silicon, green = ITO, white background = silica, dark blue = air.

(b) Schematic view of fabricated MZI structures. Upper: TM grating, lower: TE grating.

(c) Deposited structure.

(d) Deposited structure: detail.

Figure 16: The simulated and fabricated structures. The simulated region is limited to $3\,\mu m \times 2\,\mu m$ since the modes are confined within a distance $\sim \lambda$.

authors merely use a silicon waveguide with a thin layer of an insulator and ITO deposited on top [17, 18, 19]. Others design a slot waveguide with ITO in the slot, leading a much higher confinement of the optical mode both because of the ENZ-effect and the slot waveguide characteristics [7, 20]. High-permittivity insulators such as HfO_2 are often used between the ITO and the metal contacts to increase the allowed amount of accumulated charge before the structure breaks down. Another recent work placed an ITO slab in between two silicon slabs in a directional coupler scheme [21]. Applying a gate voltage and inducing the accumulation of electrons in the ITO leads to both extra attenuation losses and a refractive index shift. The index shift changes the effective index of the supermodes of the coupler, resulting in a changed coupling length and thus a decrease in the coupling efficiency, leading to a higher extinction ratio.

Most mentioned works assume an exponential accumulation layer of which the length is determined by the Thomas-Fermi screening length and is usually ~ 1 nm [7]. To simulate this layer, the ITO is split into two regions: bulk and accumulation layer. The accumulation layer is taken to be a few nanometers wide and an average carrier density or permittivity is assumed in the whole layer. This approximation however is not accurate and leads to overestimation of the change in the ITO, which causes overestimation of the figures of merit of a simulated modulator. Koch et. al. used the quantum hydrodynamic model (QHM) to calculate the static accumulation of charge at TCO-insulator interfaces and actually included these data in a mode solver [19]. This QHM model takes nonlinear accumulation effects, including quantum pressure of the electron gas, into account.

2.5.2 P-N junctions

Capacitive structures only allow significant index modulation in a narrow accumulation layer of around 1 nm thickness, which results in the need for an extremely confined mode at the accumulation layer. This is usually done using the ENZ-effect. Different designs for absorption modulators are proposed with figures of merit ranging from 37 to 3.7 [17, 19]. The FOM of 37 was for a TE absorption modulator where the approximated accumulation layer is used in the mode solver, whereas the FOM of 3.7 was obtained when the QHM model was implemented in the mode solver. As shown in the simulations, changing the bulk refractive index of the ITO leads to much higher figures of merit for electro-absorptive modulators. Absorption contrasts of 150 up to 200 can be obtained in simulations around the ENZ regime for both polarizations. This bulk change is achievable using junctions, as already explored for silicon modulators [22]. In contrast with the unity change that can be achieved using ITO (see figure 1b), the plasma dispersion effect in silicon only provides index shifts smaller than 10^{-1} RIU [23]. The use of ITO thus allows a significant reduction of the device's active length, allowing a higher level of integration if the optical mode overlaps enough with the ITO bulk.

The mentioned absorption contrasts of 150 and higher are under the assumption of complete and uniform depletion of electrons from a high carrier density to the low value of $3 \cdot 10^{19}$ cm^{-3}. A more realistic model takes exponential decay of the minority carrier density in the depletion region into account, which is however more difficult to simulate in a mode solver based on uniform slabs. As a p-type material, a degenerate semiconductor with a wide band gap is needed. The wide band gap should make sure that the light in the waveguide is not able to excite electrons from the valence band to the conduction band. The degeneracy is needed in order to limit the size of the junction. A rough measure of the amount of needed material is to assume complete depletion and state that every electron in the ITO should fill a hole in the p-type material. Silicon can be degenerately doped to have hole concentrations up to 10^{20} cm^{-3}, resulting in an index shift of the order of 10^{-1} [23] and bandgap narrowing around 150 meV [24]. Silicon will still remain transparent at $1.55\,\mu\mathrm{m}$ at this doping level. Another possible material is LaCuOSe, which is considered to be a promising candidate in the

search for a degenerate, wide band gap p-type TCO with both large hole concentrations and large hole mobility [25]. The development of such a material would open the gates to "transparent electronics". Mg-doped LaCuOSe is reported to reach a hole concentration of $2 \cdot 10^{20}$ cm^{-3} [26]. Scanlon et. al. have theoretically shown that Sr, and not Mg is the optimal dopant for LaCuOSe [25]. If it is possible to deposit a layer of LaCuOSe on top of ITO, a high-depletion junction could be made with reasonable dimensions and the high extinction ratios from the simulations could be realised.

2.5.3 N$^+$-N junctions

The carrier density and conductivity in ITO depend on the concentration of tin atoms and oxygen vacancies in the crystal lattice. The Fermi-level lies in the conduction band and rises with increasing free electron densities. As mentioned in section 2.4.1, a 0.5 eV shift of the work function can be achieved when changing the tin content of the ITO. Due to the automatic venting of the sputtering machine and the oxidation of the upper layer, depositing two layers of ITO with different tin contents in subsequent sputtering steps will not yield a good junction. Somehow, the change should be implemented in a single sputtering step. A possibility might be to use a variable oxygen concentration in the depositing atmosphere during a single step. If annealing is necessary afterwards, it should be done at temperatures low enough to prevent the diffusion and equal spreading of the oxygen.

2.5.4 Carrier generation by UV

As already proposed by Chen et. al. in 1991, it is possible to change the bulk carrier density in ITO by injecting UV light in the ITO [27]. For a band gap of $\geq$ 3.5 eV, light with a wavelength of 350 nm or lower should be used. The speed of the modulator would be determined by the excess majority carrier lifetime, which is typically strongly dependent on the excess concentration.

2.6 Switching using ITO

2.6.1 Thermo-optic switching

ITO's high conductivity suggests it could be used as an efficient heater near a silicon waveguide. Silicon's thermo-optic coefficient around $1.55\,\mu\mathrm{m}$ is $1.8 \cdot 10^{-4}$ K^{-1} at room temperature and rises to $2.3 \cdot 10^{-4}$ K^{-1} around 600 °C [28]. The wavelength shift should have the same sign as the thermo-optic coefficient, which is positive for both silicon and silica [28, 29]. Sending a current through the ITO strip and generating Joule losses, the effective index of the guided mode could be changed. Heating the long arm of an asymmetric MZI, such as those in figure 16b, would lead to a resonance shift towards higher wavelengths if the modal index is increased. However, the experimental data show the opposite, a resonance shift towards lower wavelengths when the voltage over the ITO is increased, meaning that the effective index of the mode is being decreased. These data are discussed in section 3.

2.6.2 Non-volatile switching

Not only do the measurements indicate a resonance shift opposite to the direction that could be expected from the thermo-optic effect in silicon, also irreversible changes are observed when subsequently increasing and decreasing the voltage, or turning it off. The resonance wavelength does not return completely to its original value. Understanding the origin of this behaviour and controlling it would mean that ITO could enable non-volatile switching, i.e. the properties of the switch are not reset when the voltage returns to zero.

3 Experimental work

3.1 Influence of the annealing temperature on the resistivity

Three groups of samples were made and characterized by the fabrication team in different processing conditions. In this section, the electrical properties of the ITO are shown as a function thereof. I-V curves were measured using a four point probe set up. The sheet resistance and resistivity are obtained from the I-V curve using the following formulae:

$$R_s = \frac{\pi}{\ln 2} \cdot \frac{V}{I} \tag{12}$$

$$\rho = R_s \cdot t \tag{13}$$

In the first set of samples (label 1), ITO was deposited on quartz. The working gas during deposition consisted of 8 vol% of O_2 in argon. The resulting thickness after 4 minutes of sputtering was 90 nm. Annealing steps were always 30 minutes long in a N_2-atmosphere. In this set, annealing temperatures varied from 300 °C to 800 °C. The second set of samples (label 2) was deposited in the same way as set 1, but now the annealing temperatures were lower: from 20 °C to 380 °C. The thickness was 92 nm. Finally, a third batch of samples (label 3) was deposited in an Ar-only atmosphere and annealed in the same temperature range as set 2. The thickness of this set was 115 nm, $\sim$25 nm thicker than with the mixed gas. The resistivity measurements of all samples are given in figure 17. Also shown on this plot is the resistivity as measured using a two probe method on our sample, as described in section 3.2. Our sample was fabricated in the same conditions as set 1, with annealing at 300 °C. Above 200 °C, a sudden drop in resistivity related to the increasing crystallinity is observed. A minimal resistivity is found at a temperature around 400 °C. A similar result was reported by Guillén and Herrero for annealing in an N_2 atmosphere [30]. The nitrogen can bind to the oxygen, resulting in more oxygen vacancies. The resistivity as measured on our sample lies below these values, close to the minimal value at 400 °C.

3.2 I-V relation

The electrical resistance of the ITO was measured for ITO strips of different lengths. The I-V diagrams and the resistance as a function of the ITO length are given in figure

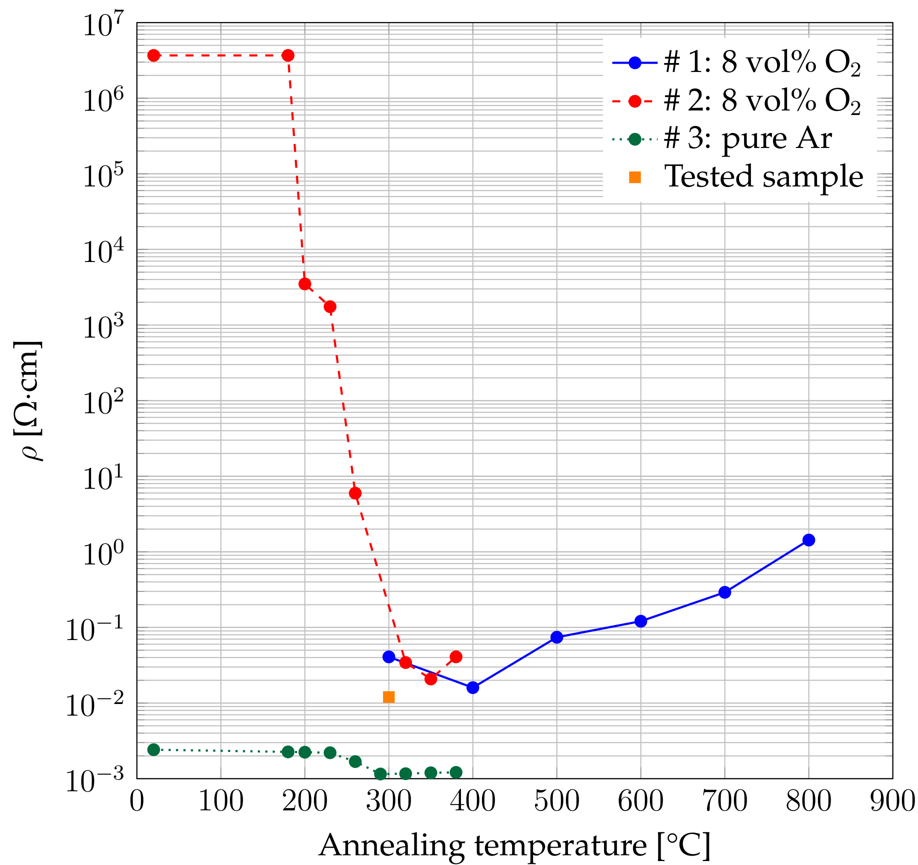

Figure 17: Resistivity measurements on three sets of samples as a function of annealing temperature. All annealing steps were 30 minutes long.

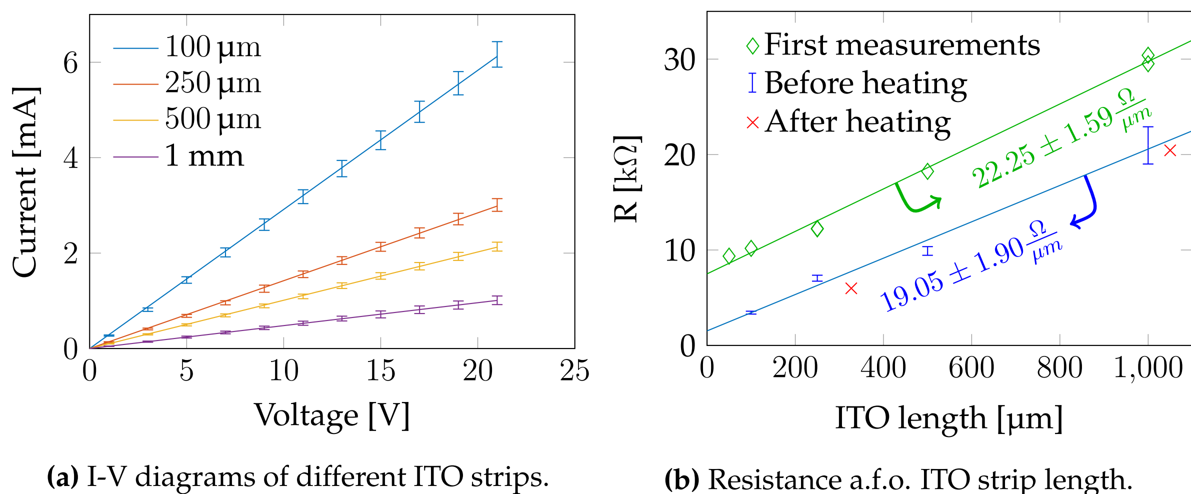

(a) I-V diagrams of different ITO strips.

(b) Resistance a.f.o. ITO strip length.

Figure 18: Electrical properties of ITO before and after long term heating. The 250 µm strip was heated for 60 minutes with a power of 100 mW (27 V), the 1 mm strip was heated for 5 hours with a power of 11 mW (15 V).

18. Measurements made on the sample by other researchers before the start of this

work are shown in green diamonds. Every point in figure 18a is the average of 4 measurements. The error bars indicate the standard deviation. The "length" of the deposition denotes the straight part, parallel to the waveguide. When measuring the current through a strip, the contacts are put in the squares, as close to the straight part as possible. The resistance obtained from all 4x4 measurements were used to fit the resistance over length to a linear function $\frac{\partial R}{\partial L} \cdot L + a$. The slope is an estimate for the resistance per unit length of the ITO. The interception with the y-axis is the result of the DC probes being placed slightly away from the straight strips. This extra distance can be estimated as the ration of the intercept value and the slope. The slopes of the RL-fittings are indicated in figure 18b.

$$\Delta l = (80 \pm 57)\ \mu m \tag{14}$$

The target thickness of the deposition was 100 nm, however the real deposited thickness is only about 92 nm and moreover a small surface layer is oxidized after the sputtering. Assuming the thickness is 92 nm and the width of the strip is $67\,\mu\text{m}$, the resistivity of the ITO becomes:

$$\rho = \frac{R}{l} \cdot A = (1.17 \pm 0.12) \cdot 10^{-2}\ \Omega \cdot cm \tag{15}$$

The measured resistivity has not reasonably changed after all the measurements and heating.

3.3 Influence of current on the optical response

The transmission characteristics of the MZI structures from figure 16b are investigated when different voltages are applied over the ITO strips. In the following, the voltage was always applied over the strips on the long arms of the MZIs. A tunable laser [Agilent 8164B] was used as a light source to sweep over a wavelength range around two times the FSR in order to have enough data to get an accurate fitting. The laser output (0 dBm) was passed through a polarization shifter and directed through standard single mode fiber towards the grating couplers on the sample. The sample was fixed to a translation stage through a vacuum suction tube. Another fiber carried the light towards a photodiode [Thorlabs PM 320E]. The power was supplied by a voltage source [Agilent E3647A] and a multimeter [Keysight 34410A] was used to measure the current flow. The response of the MZI can be written as:

$$\frac{P_{out}}{P_{in}} = \frac{1}{4} A_{grating} A_0^2 \cdot \left(1 + A_\Delta^2 + 2A_\Delta \cos(\phi)\right) \tag{16}$$

$$A_0 = \exp\left(-\kappa_s L_s - \kappa_i(0) L_i)\right) \tag{17}$$

$$A_\Delta = \exp\left(-\kappa_s \Delta L - \Delta\kappa_i L_i\right) \tag{18}$$

$$\phi = \beta_s \Delta L + \Delta\beta_i L_i \tag{19}$$

Here, L_s and L_i indicate the length of the silicon-only waveguide in the upper arm and the length of the ITO-on-silicon parts, respectively. ΔL denotes the asymmetry in the

silicon waveguide length. The silicon waveguide losses are assumed to be independent of the voltage and denoted using α_s. The losses in the ITO-on-Si waveguides do depend on the voltage and are denoted using $\alpha_i(0)$ in the case $V = 0$. $\Delta\alpha_i$ equals the difference in loss coefficient due to the applied voltage: $\Delta\alpha_i = \alpha_i(V) - \alpha_i(0)$. The equation (16) can be rewritten as a function of frequency and the optical response (shown a.f.o. wavelength in figure 19) can be fitted using a first order Fourier series:

$$y = a_0 + a_1 \cos(w \cdot x) + b_1 \sin(w \cdot x) \tag{20}$$

$$= a_0 + \sqrt{a_1^2 + b_1^2} \cos\left(w \cdot x - \arctan\left(\frac{b_1}{a_1}\right)\right) \tag{21}$$

In order to make sure the resonance frequencies are estimated correctly, the 10% largest and smallest data points are given a relative weight of 10. From the fitting, certain characteristics such as free spectral range (FSR) and extinction ratio are easily determined:

$$\text{FSR} = \Delta f = \frac{2\pi}{w} = \frac{c}{n_{g,s}\Delta L + \Delta n_{g,i} L_i} \tag{22}$$

$$\text{ER} = \frac{a_0 + \sqrt{a_1^2 + b_1^2}}{a_0 - \sqrt{a_1^2 + b_1^2}} = \left(\frac{1 + A_\Delta}{1 - A_\Delta}\right)^2 \tag{23}$$

To link the information from the fitting to the parameters of interest, the FSR and ER are deduced from equations (16) to (19). These calculations are shown in appendix **??**. From the extinction ratio, the relative change with voltage of the loss coefficient of the mode in the ITO-on-silicon waveguide ($\Delta\alpha_i$) can be determined. The FSR can be used to link a shift of the resonance frequency to a relative change in the effective index and group index of the ITO-on-silicon waveguide. We will only investigate the effective index, under the approximation that only the waveguide section below the ITO is influenced. Heating effects will of course extend further.

$$\frac{\Delta\phi}{2\pi} = \frac{\Delta f}{\text{FSR}} = \frac{-\Delta\lambda}{\text{FSR}_\lambda} \tag{24}$$

$$\Delta\phi = \frac{2\pi f \Delta n_i L_i}{c} = \frac{2\pi}{\lambda}\Delta n_i L_i \tag{25}$$

$$\Rightarrow \Delta n_i = \frac{\Delta f}{f} \cdot \frac{c}{\text{FSR} \cdot L_i} = \frac{\lambda\Delta\lambda}{\text{FSR}_\lambda \cdot L_i} \tag{26}$$

From equation (22) and figures 19 and 20, we can compare the theoretically expected FSR and the measured value. The group index of the TM mode in the silicon waveguide at 1550 nm is 3.8325 according to simulations and the path length difference is 2 x 470 μm. Assuming that the difference in group index of the ITO-on-Si waveguide is negligible, the expected FSR is 0.667 nm. The mean FSR of all measurements was 0.668 nm with a standard deviation of 7.0 pm, corresponding very well with the simulated value. For the fundamental TE mode, the group index at 1565 nm is 4.1899 according to the simulation, leading to an expected FSR of 0.610 nm. The first measurement at 0V of the TE MZI shows an FSR of 0.609 nm, again in agreement with the simulation.

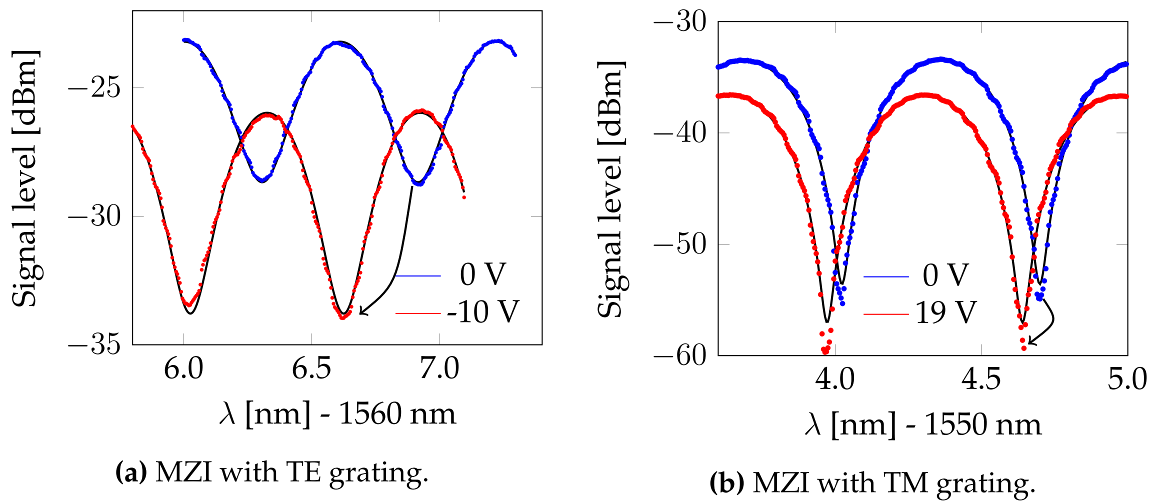

(a) MZI with TE grating.

(b) MZI with TM grating.

Figure 19: Shift in the optical response of the MZI structures. The shift depends on voltage and time.

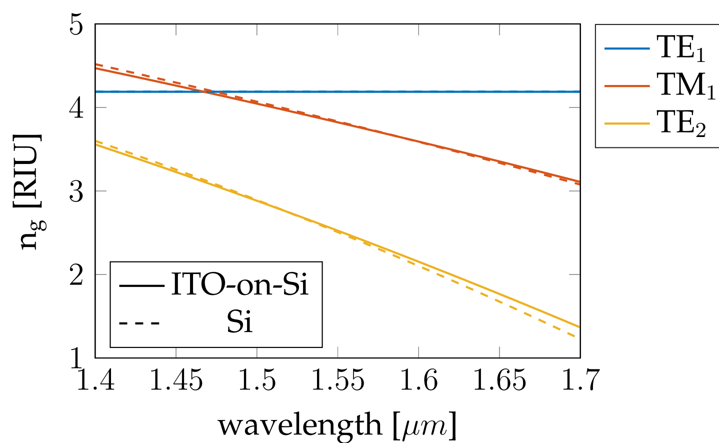

Figure 20: Waveguide dispersion with and without ITO layer on top, simulated using the structure from figure 16 for the Drude parameters from table 1.

In figure 21, the ITO's response to an applied voltage is shown as the shift of the effective index of the mode versus the dissipated power in the ITO. No clear trends can be identified. The response is not linear, irreversible and is different in every sweep. The shift is towards lower modal indexes, contrary to what could be expected from the thermo-optic effect. The shift is one order of magnitude larger in the waveguide with TE-optimized gratings. For the TE MZI, a smaller first sweep was done. Some degree of repeatability is seen, but the response is not completely the same as the first time. Although the two curves start at the same point in this graph, the starting resonance frequency the same as in the previous run, only the shift of the resonance frequency relative to its original position on each day was measured. The structure seems to be changed permanently. The response does not return to its original position and appears to stay there. This was checked with three measurements, each spaced 10 minutes apart, for the TM MZI after its voltage sweep.

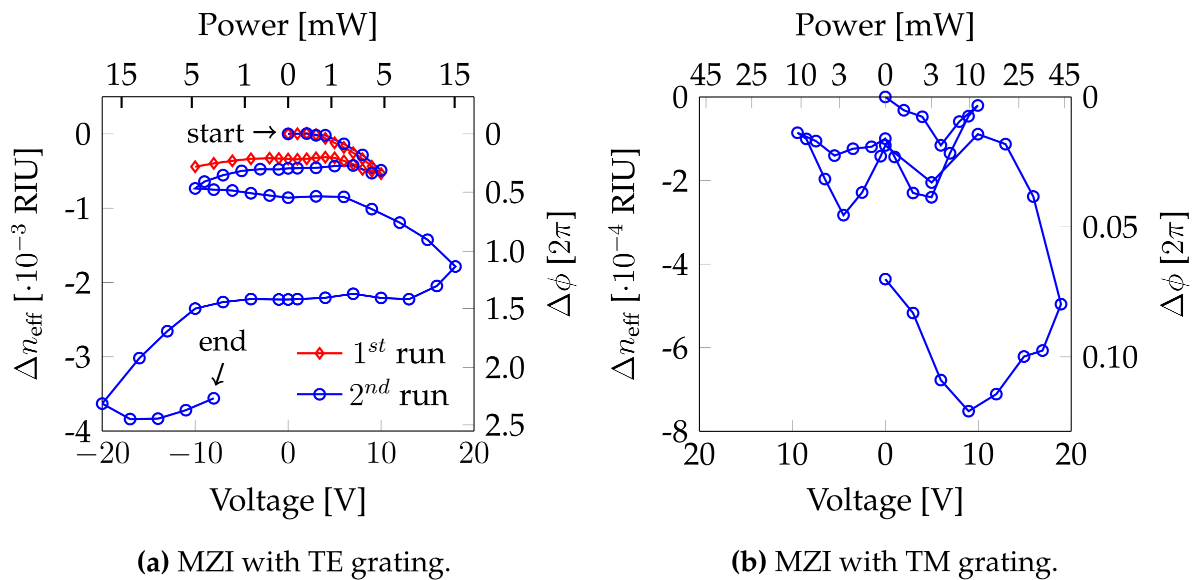

(a) MZI with TE grating.

(b) MZI with TM grating.

Figure 21: Effective index shift of ITO-on-silicon waveguides as a function of dissipated power in the ITO. The wavelength step of the laser was 5 pm. Every measurement took around 3 minutes to complete and was immediately followed by the next measurement.

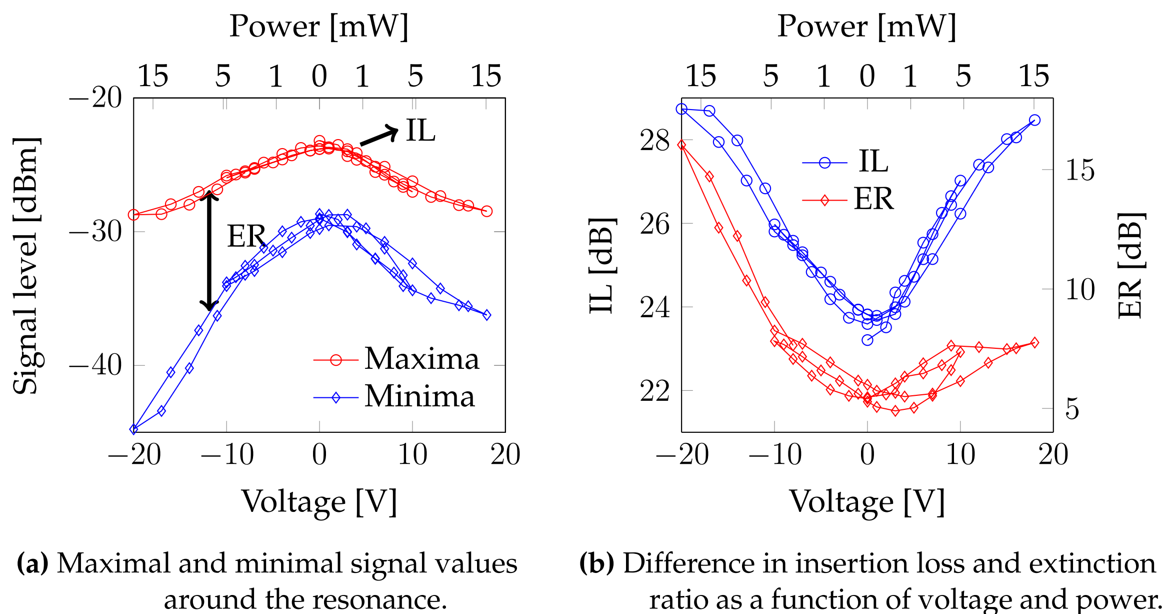

(a) Maximal and minimal signal values around the resonance.

(b) Difference in insertion loss and extinction ratio as a function of voltage and power.

Figure 22: Losses in the MZI with a TE grating.

In figure 22a, the signal boundaries (lowest and highest intensities) are plotted as a function of the applied voltage. The insertion loss and extinction ratio can be deduced from it, and they are given as well in figure 22b. The absorption losses increase with voltage, as shown by the IL. Contrary to what could be expected, the ER increases with

higher losses. Even a large increase of the ER can be seen in the last part of the voltage sweep, to -20 V and back. On top of the thermo-optic effect in silicon, clearly there is some other slow effect that affects the device performance. Long term heat treatments by current injection were suggested to check if the ITO's conductivity and hence it's optical properties are influenced by the heat in a way that might explain the measurements. If permanent changes are indeed induced, the heat treatment was hoped to lead the whole structure to a stable configuration. Spread over two days, the lower arm of the TE MZI was heated with a power around 11 mW (15 V) for about 400 minutes. During this heat treatment, the resonance shift was monitored to see if it would converge to a final value. Figure 23 shows both the resonance shift and the speed of the shift. The shifting speed was determined using a simple first order finite differences approximation.

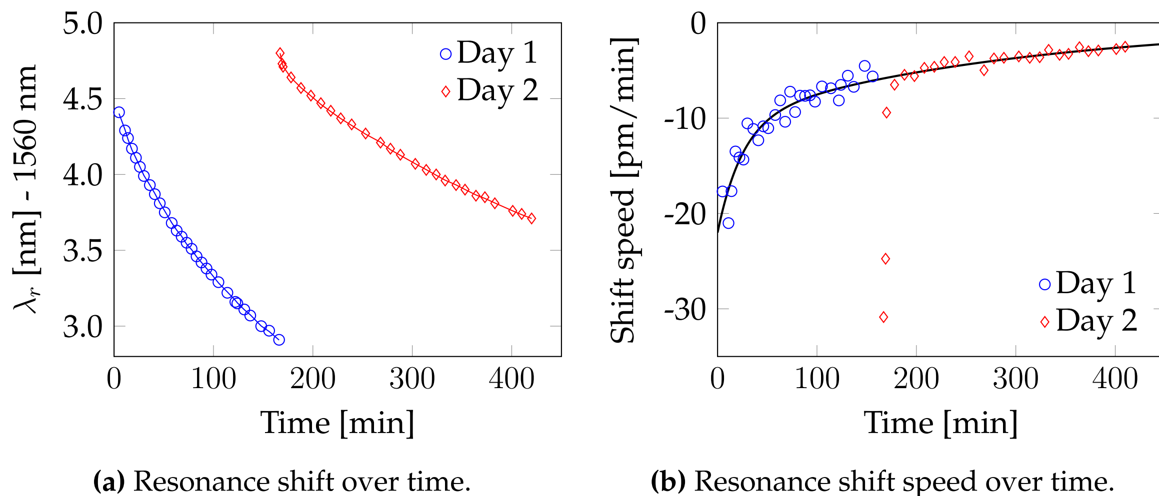

(a) Resonance shift over time.

(b) Resonance shift speed over time.

Figure 23: Heat treatment of the ITO in the TE MZI by applying 15V over the ITO for several hours. The derivatives for the first two samples of Day 2 aren't used in the calculation of the fitting.

It can be noted that, although the measurement was interrupted halfway, the shifting speed was not reset to the initial value of day 1. This shows that the system is indeed changed permanently by the heat. The shifting speed decreased continuously, but the resonance did not reach a final stable position in the measured time. The shifting speed was fitted to the sum of two exponentials since on both days the shift over time appears to be exponential. If the shift would follow this trend, another heat treatment might lead to a stable configuration. After this heating, a new voltage sweep below 15 V was done in the TE MZI. The results are displayed in figure 24 and for comparison, the curve from figure 19a is also shown in the background (dotted curve). The resonance shift is still present, although it is one order of magnitude smaller. Also remarkable is that the extinction ratio now decreases when the overall losses increase. This could be explained by the fact that the previous researcher had made measurements whereby he applied voltages over the ITO strip in the short arm of the TE MZI. These measurements could have caused an increase in optical loss in this strip. Afterwards, applying

voltages over the ITO strip in the long arm of the MZI, the losses became more similar and this offset was compensated. During the voltage sweep, a general shift to higher ERs can be noted. The insertion losses remain approximately reversible.

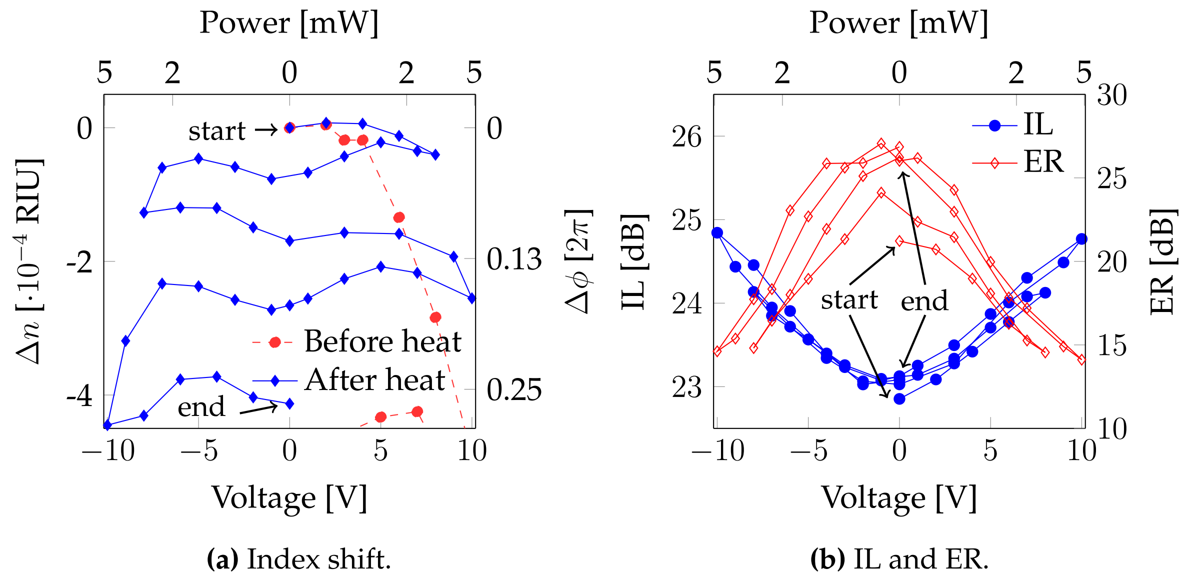

(a) Index shift.

(b) IL and ER.

Figure 24: Voltage sweep response after the heat treatment. The wavelength step was doubled to 10 pm. The datapoints were now on average obtained every 2'20".

4 Discussion

4.1 Hypotheses

The shift towards lower wavelengths indicates a decrease of the modal index, as shown before. This is contrary to what could be expected from the thermo-optic effect in silicon. The origin of this effect has not yet been fully identified. In what follows, some hypotheses are proposed that may explain some of the observed results. In chapter 2, the fabrication process of the sample was described, because the characteristics of the used materials are relevant.

Applying high voltages over the ITO results in substantial heating. This heat affects all materials around the waveguide: the ITO, the HSQ, the silicon and the bulk silica. The actual temperatures in the ITO strips were not measured, however the power levels could cause temperatures of a few hundreds °C, making it possible to exceed the annealing temperature. Such high temperatures cause temporary and possibly also permanent changes in the materials. The temporary change includes thermal expansion and the thermo-optic effect in all materials. This effect works in very short time intervals, as compared to the heating steps that took several hours, and is not the only effect in play. Permanent changes could occur in the ITO and in the HSQ layer. The silicon waveguide and oxide substrate are assumed to remain unchanged. If the temperature in the ITO approaches or exceeds the annealing temperature for more than

20 minutes, a new ”annealing step” might take place and diffusion of oxygen could affect the ITO. This would be seen in both the electrical and the optical properties. In this sample, however, no obvious decrease of the resistivity was noticed after all the heating steps. The resistivity values that were obtained at three different times are not sufficiently distinctive to confirm a change. The error margins are too large and the values depend on placement of the DC probes. Optical transmittance and reflectance measurements on the sample were no longer possible since the surface was not completely covered in ITO. During the annealing, not only the ITO but also the HSQ layer underwent structural changes. At 300 °C, Yang and Chen predict a structural network change in the HSQ, however the structure will remain porous [13]. If in our heating processes the temperatures were increased above 350 °C or 450 °C, the porous structure will respectively undergo thermal dissociation or collapse and lose its porosity. This will deform the surface on which the ITO is deposited and bring the heat source closer to the silicon waveguide. In the collapsing process, the refractive index of the HSQ would become closer to that of thermally grown silica. All these effects would however increase the modal index and not lower it, as measured experimentally.

For the hypotheses, we make the approximation that HSQ's refractive index remains the same in the whole heating process to make the analysis easier. The only components that are affected are the silicon and the ITO. Silicon's refractive index will increase around 0.001 RIU at temperatures of a few hundreds of degrees, but this increase is fast and cannot lead to a constant shifting over several hours. Two distinct mechanisms are proposed that might cause the observed effects:

1. During the heating, the ITO's refractive index drops constantly, thus lowering the modal index. After several hours of heating, the ITO becomes more stable and the shift speed lowers.
2. During the heating, the ITO's refractive index does not change at all, but the HSQ keeps collapsing. If the ITO's refractive index is below that of silica, the modal index will keep decreasing while the ITO approaches the silicon waveguide. The shift speed lowers since the maximal volume change of the HSQ is finite.

4.2 Problems

For small changes, the relation between the modal index and the refractive indices of the different materials is approximately linear. In figure 25, the refractive index change in ITO that is needed to compensate the thermo-optic shift of 0.001 RIU in silicon, is shown for different spacer sizes. However, to cause the observed resonance shift over several times the FSR, a multiple of the indicated shift is needed. This is certainly not possible for a spacer distance of 200 nm. Furthermore, the effect of an index change of the ITO will influence the TM mode more strongly, while at first the observed index shifts for the TM MZI were an order of magnitude smaller than those of the TE MZI. This is an issue in hypothesis # 1. On the other hand, it cannot be excluded that other researchers have induced changes in the TM MZI prior to the measurements reported

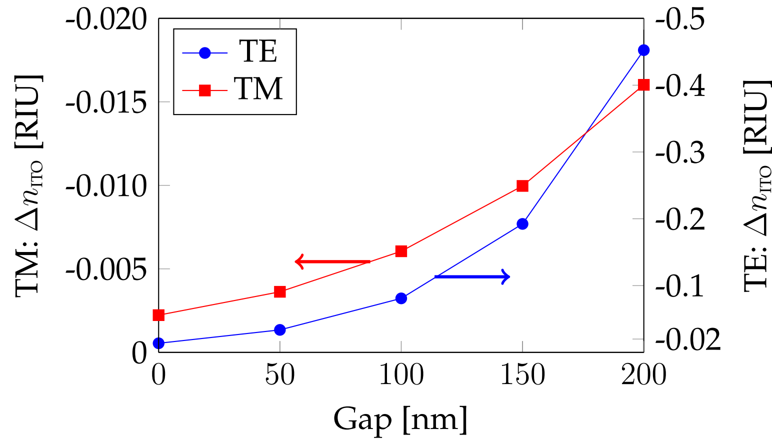

Figure 25: Needed index change in ITO to compensate a thermo-optic shift of 0.001 RIU in silicon a.f.o. spacer size.

here.

In the case where the ITO layer approaches the silicon waveguide through the collapsing of HSQ's porous structure, the overlap of the optical mode with the ITO and the air above would increase. Again, this would influence the modal index of the TM mode more than that of the TE mode. In figure 26, the gap dependency of the modal index is shown for both polarizations and different values for ITO's refractive index. The modal index of the TM mode always decreases with smaller gaps. For the TE mode, this is only the case when ITO's refractive index is around 1.5 or lower. In figure 27, ITO's refractive index is plotted as a function of the two Drude parameters, N and γ. Contours are shown with the for combinations with the same refractive index and two solid lines indicate the combinations resulting in the measured resistivity and the one expected from literature. If our resistivity measurements can be used to estimate the Drude parameters, it is obvious from figure 27 that hypothesis # 2 cannot be used to explain the observed results. With the measured resistivity, it is impossible to have a refractive index around or smaller than 1.5 RIU. It could however be possible that due to damage in the HSQ, the ITO is dislocated and deformed, which increases the resistivity. On the other hand, the resistivity is lower than the one measured right after the fabrication.

4.3 Future lines

To further test the proposed hypotheses, a few experiments are suggested. Since we're assuming permanent changes, the best practice would be to start with a fresh sample, fabricated in the same way as the one reported here.

1. Perform a scanning electron microscopy (SEM) scan on the old sample to check for structural deformation due to the heat. This would confirm the assumption of the collapse of the HSQ.

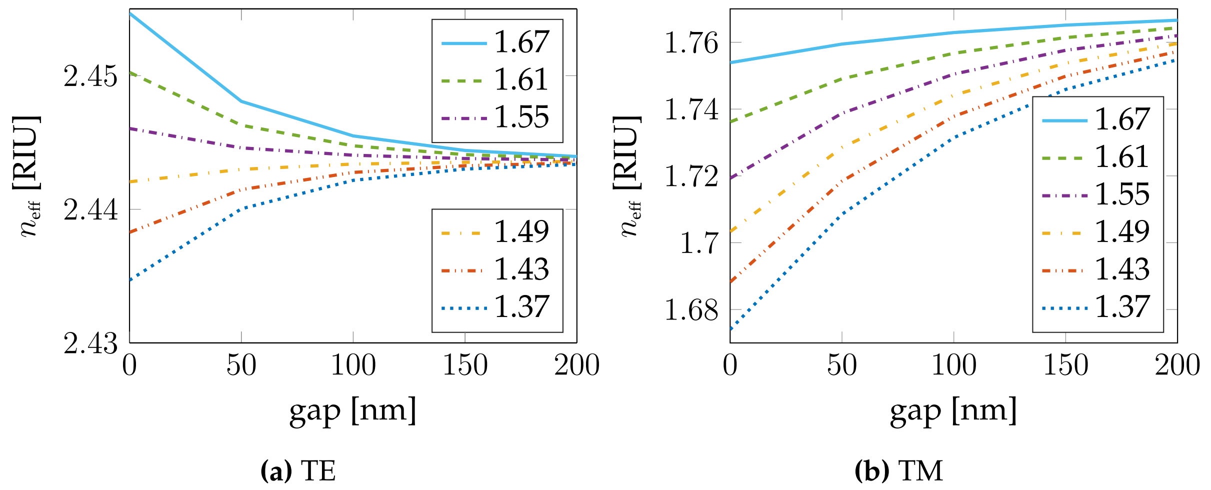

(a) TE **(b)** TM

Figure 26: Gap dependency of the modal index for different refractive indices of ITO.

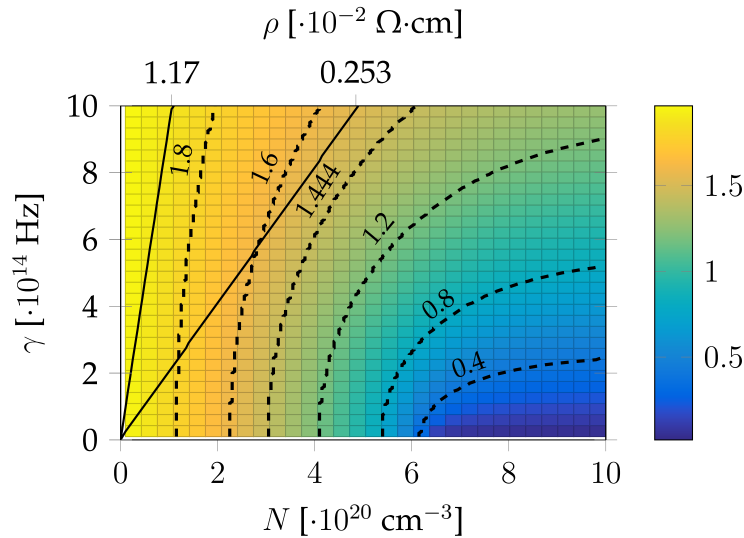

Figure 27: ITO's refractive index at 1550 nm a.f.o. the Drude parameters. The dashed lines are contours of equal refractive index, which is indicated with a label. The solid lines connect points with the same resistivity, which is indicated on the upper x-axis.

2. Since both the ITO and the HSQ are questioned in the hypotheses, it might be useful to replace those with other materials. A sample with PECVD deposited silica and ITO electrodes and a sample with HSQ and metal electrodes could be fabricated to see how the MZI response will be.

3. Use a sample with bare HSQ and ITO layers to investigate the volume and refractive index change in the HSQ layer through ellipsometry experiments before and after annealing and after a long term current injection. Also the changes in the ITO layer (thickness, roughness, resistivity) can be monitored.

4. After a heating step, monitor the optical response over a long time to see if the

resonance keeps shifting or stays fixed at the position it returns to right after turning of the heat.

5 Conclusion

In this work, ITO-integrated waveguide structures have been simulated for optical modulation. Significantly higher figures of merit are expected for absorptive modulators exploiting bulk carrier density tuning in ITO, as compared to those based on capacitive carrier accumulation in a MOS-structure. In a junction, absorption contrasts up to 200 can be reached. The assumptions are made that the depletion region can extend over the whole ITO layer, the electron scattering frequency remains the same and the P-type material on top of the ITO does not influence the optical mode significantly. To create P-N junctions, degenerately P-doped silicon and LaCuOSe are proposed as P-type materials, based solely on their transparency at 1550 nm and the achievable hole densities. Refractive modulator structures based on the plasma-dispersion effect in ITO have also been simulated. The TM structure has an active length below 2 μm and the TE structure is insensitive to variations of some of its parameters.

More investigation is needed to identify the causes of the observed resonance shift, opposite to the thermo-optic effect. The first materials to investigate are the HSQ oxide and the ITO. SEM images should be taken and ellipsometry experiments should be performed in different stages of the fabrication and lifecycle of the device in order to better characterize the occurring changes.

Acknowledgements

First of all, I would like to express my thanks to my supervisor, prof. Pablo Sanchis, who gave me guidance during this thesis and kept me on track, focussed on the goal. I enjoyed our fruitful meetings.

Besides my supervisor, I would also like to thank Ir. Juan Hurtado, for having the patience to explain the fabrication process time after time and Ir. Álvaro Rosa and Ir. Luis Sanchez for their help with the experiments.

Finally, Bert De Deckere and Laurens Meeus deserve their place on this list, for being always available for a chat and a scientific discussion. Their inputs and comments are always valued and appreciated.

Camiel Op de Beeck, June 2016

References

[1] M. Bender, W. Seelig, C. Daube, H. Frankenberger, B. Ocker, and J. Stollenwerk. Dependence of oxygen flow on optical and electrical properties of dc-magnetron sputtered ITO films. *Thin Solid Films*, 326(1-2):72 – 77, 1998.

[2] C. Guillén and J. Herrero. Influence of oxygen in the deposition and annealing atmosphere on the characteristics of ITO thin films prepared by sputtering at room temperature. *Vacuum*, 80(6):615 – 620, March 2006.

[3] F. Michelotti, L. Dominici, E. Descrovi, N. Danz, and F. Menchini. Thickness dependence of surface plasmon polariton dispersion in transparent conducting oxide films at $1.55\,\mu m$. *Opt. Lett.*, 34:839–841, 2009.

[4] P. P. Edwards, A. Porch, M. O. Jones, D. V. Morgan, and R. M. Perks. Basic materials physics of transparent conducting oxides. *Dalton Trans.*, (19):2995–3002, 2004.

[5] F. Neuman, Y. A. Genenko, C. Melzer, S. Yampolskii, and H. von Seggern. Self-consistent analytical solution of a problem of charge-carrier injection at a conductor/insulator interface. *Phys. Rev. B Condens. Matter*, 75(20), 2007.

[6] E. D. Palik. *Handbook of Optical Constants of Solids*, volume III. Academia press, 1998.

[7] J. Baek, J. You, and K. Yu. Free-carrier electro-refraction modulation based on a silicon slot waveguide with ITO. *Opt. Express*, 23(12):15863–15876, Jun 2015.

[8] Z. Ma, Z. Li, K. Liu, C. Ye, and V. J. Sorger. Indium-tin-oxide for high-performance electro-optic modulation. *Nanophotonics*, 4(1):198–213, June 2015.

[9] Y. Saton, T. Ashida, N. Oka, and Y. Shigesato. Carrier density dependence of optical band gap and work function in Sn-doped In_2O_3 films. *Applied Physics Express*, 3(6):061101, 2010.

[10] Scott H. Brewer and Stefan Franzen. Calculation of the electronic and optical properties of indium tin oxide by density functional theory. *Chemical Physics*, 300(1-3):285 – 293, 2004.

[11] M. H. Rein, J. Mayandi, E. Monakhov, and A. Holt. Annealing of ITO films sputtered with argon and oxygen. In *EU PVSEC Proceedings*, volume 26, pages 2608–2612. European Photovoltaic Solar Energy Conference and Exhibition, 2011.

[12] Chih-Hao Yang, Shih-Chin Lee, Suz-Cheng Chen, and Tien-Chai Lin. The effect of annealing treatment on microstructure and properties of indium tin oxides films. *Materials Science and Engineering: B*, 129(1 - 3):154 – 160, 2006.

[13] Chang-Chung Yang and Wen-Chang Chen. The structures and properties of hydrogen silsesquioxane (HSQ) films produced by thermal curing. *J. Mater. Chem.*, 12:1138–1141, 2002.

[14] S. Lis, R. Dylewicz, J. Mysliwiec, A. Miniewicz, and S. Patela. Application of flowable oxides in photonics. *Materials Science Poland*, 26(1):189–194, 2008.

[15] Z. Min, C. Baoqin, X. Changqing, L. Ming, and N. Jiebing. Study of process of HSQ in electron beam lithography. In *Nano/Micro Engineered and Molecular Systems (NEMS)*, pages 1021–1024, Jan 2010.

[16] Public domain, retrieved in May 2016. Adapted from "T8 cubic structure of Silsesquioxane":
https://commons.wikimedia.org/wiki/File:Silsesquioxane_T8_Cube.png.

[17] Alok P. Vasudev, Ju-Hyung Kang, Junghyun Park, Xiaoge Liu, and Mark L. Brongersma. Electro-optical modulation of a silicon waveguide with an "epsilon-near-zero" material. *Opt. Express*, 21(22):26387–26397, Nov 2013.

[18] V. J. Sorger, N. D. Lanzillotti-Kimura, R. Ma, and X. Zhang. Ultra-compact silicon nanophotonic modulator with broadband response. *Nanophotonics*, 1(1):17–22, May 2012.

[19] U. Koch, C. Hoessbacher, J. Niegemann, C. Hafner, and J. Leuthold. Digital plasmon absorption modulator exploiting epsilon-near-zero in transparent conducting oxides. *IEEE Photonics Journal*, 8(1), February 2016.

[20] H. Zhao, Y. Wang, A. Capretti, L. D. Negro, and J. Klamkin. Broadband electroabsorption modulators design based on epsilon-near-zero indium tin oxide. *IEEE Journal of Selected Topics in Quantum Electronics*, 21(4):192–198, July 2015.

[21] Jin-Soo Kim and Jin Tae Kim. Silicon electro-optic modulator based on an ITO-integrated tunable directional coupler. *Journal of Physics D: Applied Physics*, 49(7):075101, 2016.

[22] A. Liu, L. Liao, D. Rubin, H. Nguyen, B. Ciftcioglu, Y. Chetrit, N. Izhaky, and M. Paniccia. High-speed optical modulation based on carrier depletion in a silicon waveguide. *Opt. Express*, 15(2):660–668, Jan 2007.

[23] R. Soref and B. Bennett. Electrooptical effects in silicon. *IEEE Journal of Quantum Electronics*, 23(1):123–129, Jan 1987.

[24] S.C. Jain and D.J. Roulston. A simple expression for band gap narrowing (BGN) in heavily doped Si, Ge, GaAs and GeSi strained layers. *Solid-State Electronics*, 34(5):453 – 465, 1991.

[25] David O. Scanlon, John Buckeridge, C. Richard A. Catlow, and Graeme W. Watson. Understanding doping anomalies in degenerate p-type semiconductor LaCuOSe. *J. Mater. Chem. C*, 2:3429–3438, 2014.

[26] H. Hiramatsu, K. Ueda, H. Ohta, M. Hirano, T. Kamiya, and H. Hosono. Wide gap p-type degenerate semiconductor: Mg-doped LaCuOSe. *Thin Solid Films*, 445(2):304 – 308, 2003.

[27] Ray T. Chen, Daniel P. Robinson, Huey T. Lu, Lev S. Sadovnik, and Winston Ho. Indium tin oxide single-mode waveguide modulator. In *Proc. SPIE*, volume 1583, pages 362–374, 1991.

[28] F. G. Della Corte, M. Esposito Montefusco, L. Moretti, I. Rendina, and G. Cocorullo. Temperature dependence analysis of the thermo-optic effect in silicon by single and double oscillator models. *Journal of Applied Physics*, 88(12):7115–7119, 2000.

[29] T. S. El-Bawab. *Optical Switching*, chapter 4, page 112. Springer, 2006.

[30] C. Guillén and J. Herrero. Structure, optical, and electrical properties of indium tin oxide thin films prepared by sputtering at room temperature and annealed in air or nitrogen. *Journal of Applied Physics*, 101(7), 2007.

A Publications

Integration of indium tin oxide on silicon for enabling electro-optical functionalities

Camiel Op de Beeck, Alvaro Rosa, Luis David Sanchez, Juan Hurtado, Pablo Sanchis*

Nanophotonics Technology Center, Spain

*pabsanki@ntc.upv.es

ITO has since long been used for transparent electrodes in opto-electronic applications such as photovoltaics and display technology because of its transparency to visible and near-IR light. This transparency can also be exploited to integrate ITO on silicon waveguides for modulation and switching at the 1550 nm telecom wavelength. For wavelengths beyond 1 µm, ITO's permittivity can be described using a Drude model [1]. Since the plasma frequency of ITO is in the near-IR range, changes in the carrier density can lead to a refractive index shift greater than unity [2]. This strong manifestation of the plasma dispersion effect makes ITO so interesting for modulation. Until now, most proposed ITO-based absorption modulators used a MOS structure to accumulate charges capacitively and change the permittivity drastically in this layer. Since this layer is only a few nanometers long, very high confinement of the optical mode is needed to increase their interaction and reduce the structure's footprint. We have simulated structures for absorption modulation under the assumption that the bulk carrier density in the ITO can be tuned, for instance using P-N or N^+-N junctions. For P-N junctions, a transparent, degenerate p-type semiconductor is needed. Degenerately doped silicon and the new promising p-type transparent conducting oxide LaCuOSe are candidates. Mg-doped LaCuOSe is reported to reach a hole density of 2.10^{20} cm^{-3} with a relatively high hole mobility [3]. Under the assumption of complete depletion in the junctions, the absorption contrasts of our simulated absorptive modulators reach 200 for both polarizations. Refractive modulators based on P-N junctions have already been explored for silicon. However, the index shift due to the plasma dispersion effect can be up to two orders of magnitude larger in ITO than in silicon. Integration of ITO near the waveguide can lead to higher modal index modulation with a smaller device footprint. ITO's conducting properties also suggest its use as an efficient heater for thermo-optic switching. However, experiments have shown that dissipating power in the deposited ITO layers leads to nonlinear and irreversible changes in the optical properties of the waveguides (figure 1a: power through the ITO strip on the long arm of the MZI). A resonance shift has been observed when applying a voltage over the ITO (figure 1b). This shift is not reversed completely when the voltage returns to zero and thus a permanent change is induced. In contrast, the insertion losses of the structure are more reversible in this experiment (figure 1c: maximal and minimal signal value around the resonance). Although the optical properties of the waveguide are changed, the electrical properties of the ITO remain the same. Understanding the origin of this behaviour and controlling it would lead to ITO enabling non-volatile switching and furthermore might allow the tuning of the ITO integrated structures' optical response after deposition.

References

[1] F. Michelotti, L. Dominici, E. Descrovi, N. Danz and F. Menchini, Opt. Lett., 34 (2009) 839-841.

[2] E. Feigenbaum, K. Diest and H.A. Atwater, NanoLetter., 10 (2010) 2111-2116.

[3] D. O. Scanlon, J. Buckeridge, C. Richard, A. Catlow and G. W. Watson, J. Mater. Chem. C, 2 (2014) 3429-3438.

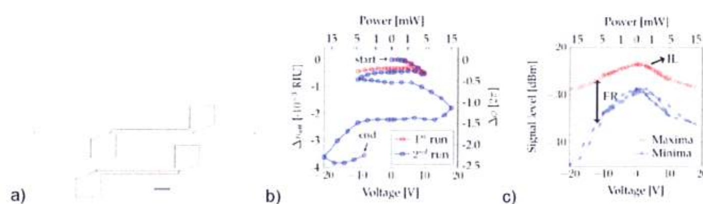

Figure 1: (a) ITO deposited onto an asymmetric MZI structure with TE gratings. Experimental change in (b) modal index, phase shift, (c) insertion loss and extinction ratio as function of the dissipated power in the ITO strip on the long arm of the MZI. Each measurement took 3 minutes to complete and was immediately followed by the next measurement.